الجمهوريـــــة الجزائريـــــة الديموقراطيـــــة الشعبيـــــة
PEOPLE'S DEMOCRATIC REPUBLIC OF ALGERIA
وزارة التـــعـليـم العـــالي والبـحث العـلـمـي
Ministry of Higher Education and Scientific Research

UNIVERSITY OF SAÏDA - DR. MOULAY TAHAR جـامعة سعيدة – د. مولاي الطاهر

Faculty of Science and Technology كلية العلوم والتكنولوجيا

Department of Materials Science قسم علوم المادة

DISSERTATION

Prepared for the purpose of obtaining a Master's degree in Physics

Specialization: Materials Physics

Title:

Synthesis, Structural Characterization, and First-Principles Study of $CuMn_2O_4$ Normal Spinel

Presented by:

Nour Elhouda KHELFAOUI

Defended on 18/06/2026 before the jury composed of:

Dr. Hayat HOCINE	University of Saïda - Dr MOULAY Tahar	President
Pr. Friha KHELFAOUI	Higher Normal School of Saida	Supervisor
Dr. Malika HACHEMAOUI	University of Saïda - Dr MOULAY Tahar	Examinator

Academic Year 2025/2026

DEDICATION

To my supervisor, Professor Khelfaoui Friha, my aunt and second mother, who has always been my source of inspiration and the role model who guided me toward this scientific path. Her dedication, wisdom, and achievements motivated me to pursue my dreams and strive for excellence.

To my beloved mother, whose endless love, sacrifices, prayers, and unwavering support have been the foundation of every success in my life. This achievement is as much yours as it is mine, and I will always be grateful for everything you have done for me.

To my dear father, whose strength, encouragement, and unwavering belief in my abilities have inspired me to persevere through every challenge. This accomplishment is dedicated to him with deep love, profound respect, and heartfelt gratitude.

To my beloved sisters, Hayam, Selsabil, Melek , Khadija, and Serine , whose love, support, and presence have filled my journey with strength and happiness.

To my dear aunt Setti, and to the lovely children Mouad, Saadia, and Jouri who have brought joy and warmth to my life.

To my classmates and friends, with whom I shared unforgettable moments, challenges, and successes.

And finally, to everyone who supported me, encouraged me, or believed in me along the way, I dedicate this achievement to you all

Acknowledgements and Gratitude

First, I would like to express my deepest gratitude to **Pr. Friha KHELFAOUI**, my supervisor, for her invaluable guidance, continuous support, and insightful advice throughout the entire duration of this work. Her expertise and encouragement have been instrumental in the realization of this dissertation. I would also like to express my sincere gratitude to **Prof. Kaid Mhamed** for giving me the opportunity to synthesize the studied material in the Laboratory of Physicochemical Studies. His support and the facilities made available to me were essential for the experimental realization of this work.

I am sincerely thankful to **Dr. Hayat HOCINE**, President of the jury, for her thoughtful remarks, constructive feedback, and for kindly accepting to preside over the defense of this dissertation.

My sincere appreciation also goes to **Dr. Malika HACHEMAOUI**, examiner, for her careful evaluation of the manuscript, insightful, and enriching discussions during the defense.

I would also like to extend my gratitude to all the faculty members, staff, and colleagues at the **University of Saïda – Dr Moulay Tahar**, especially those in the Department of Materials Science.

Finally, I thank my family and friends for their patience, encouragement, and unwavering support throughout this academic journey.

Table of contents

List of figures

List of Tables

GENERAL INTRODUCTION

GENERAL INTRODUCTION

Spinel compounds adopt the general chemical formula AB_2O_4, in which A denotes divalent cations (A^{2+}) typically occupying tetrahedral sites, while B represents trivalent cations (B^{3+}) situated in octahedral coordination within a cubic close-packed oxygen framework. These materials occur in two principal structural configurations —normal and inverse spinel—distinguished by the distribution of cations among crystallographic sites[1]. The normal spinel structure, first elucidated in 1915 by William Henry Bragg and Seiji Nishikawa [2], is characterized by A^{2+} cations in tetrahedral positions and B^{3+} cations in octahedral sites. in contrast, the inverse configuration, later described by Tom F. W. Barth and E .Posnjak[3], involves the occupation of tetrahedral sites by B^{3+} cations, while the octahedral positions are equally shared between A^{2+} and the remaining B^{3+} cations .

Owing to this structural flexibility , spinel materials exhibit diverse atomic arrangements and electronic configurations [4], which give rise to exceptional electronic , optical [5, 6], magnetic, and catalytic properties [7-10] . These properties are strongly influenced by the specific nature of the incorporated metal cation [11], their spatial distribution within the lattice , and the symmetry of the crystal structure itself .

As a consequence of this broad spectrum of functional characteristics, spinel materials have attracted considerable scientific attention [12-14] and demonstrate remarkable technological versatility. Their applications extend to magnetic data storage systems [15], high-frequency electronic devices [16], dielectric materials, transparent conducting oxides, and laser technologies[17] Additionally, they serve as key components in sensor technologies and supercapacitor electrodes [18] with further applications spanning superconductivity, biotechnology, biomedical engineering, and renewable energy systems [19-22]

Motivated by rapid advances in materials science, contemporary research has increasingly focused on ternary spinel oxides [8]. Recent density functional theory (DFT) studies on 3d transition-metal-based ternary spinels have provided valuable insight into the key parameters governing lithium-ion battery cathodes, including cation site preference, delithiation voltage, and thermodynamic stability [23] A comprehensive understanding of these factors is essential for the rational development of high-performance and practically viable cathode materials.

These ternary oxides are characterized by the presence of three distinct metal cations distributed over tetrahedral and octahedral sites within the spinel lattice. Their multicomponent nature enables a remarkably broad spectrum of tunable physicochemical

properties [24-26], making them particularly attractive for advanced energy-storage applications.

In this framework, copper manganese oxide ($CuMn_2O_4$) has emerged as a prominent spinel-type compound owing to its distinctive properties and versatile applications[27-29]. Extensive investigations have explored its magnetic characteristics and potential used in advanced functional materials. $CuMn_2O_4$ crystallizes in a spinel structure, conventionally written as $(Cu^{2+})[\ 2Mn^{3+}]O_4$, and exhibits ferromagnetic behavior [30]. Its physicochemical and magnetic properties are strongly governed by cation distribution and lattice arrangement. Furthermore, elemental substitution through doping or stoichiometric modification has been shown to significantly influence its magnetic response, thereby opening pathways for tailored material design.

To systematically investigate the intrinsic properties of this spinel compound and to explore its untapped potential, we employed first-principles calculations based on the full-potential linearized augmented plane wave (FP-LAPW) method. All computations were carried out using the WIEN2k code [31] , with exchange–correlation effects described within the Generalized Gradient Approximation (GGA) [32] This methodological approach enables reliable verification of structural stability, accurate prediction of elastic properties, and detailed elucidation of the electronic and magnetic characteristics of $CuMn_2O_4$.

The manuscript is organized into four main chapters. Chapter I provides a comprehensive overview of spinel materials, covering their fundamental principles, key physical properties, and current technological applications. Chapter II describes the theoretical framework, with particular emphasis on density functional theory and the FP-LAPW method. Chapter III is dedicated to the synthesis methods. Finally, Chapter IV presents and discusses the obtained results in detail.

The work concludes with a synthesis section summarizing the main findings, emphasizing the most significant results, and proposing concrete directions for future research, along with promising technological perspectives.

References

1. Stevanović, V., M. d'Avezac, and A. Zunger, *Simple point-ion electrostatic model explains the cation distribution in spinel oxides.* Physical review letters, 2010. **105**(7): p. 075501.
2. Nishikawa, S., *Structure of some crystals of spinel group.* Proceedings of the Tokyo Mathematico-Physical Society. 2nd Series, 1915. **8**(7): p. 199–209_1.
3. Barth, F. and E. Posnjak, *Silicate structures of the cristobalite type. I. The structure of α-carnegieite, NaAlSiO 4.* Z Kristallogr, 1932. **81**: p. 135–141.
4. Sharma, A., *Influence of different substitution metal ion on magnetic properties of Mn-Zn ferrite.* Materials Today: Proceedings, 2021. **37**: p. 3058–3060.
5. Allali, D., et al., *Electronic and optical properties of the spinel oxides GeB2O4 (B= Mg, Zn and Cd): an ab-initio study.* Journal of Nanoelectronics and Optoelectronics, 2019. **14**(7): p. 945–952.
6. Hema, E., et al., *The role of Mn2+-doping on structural, morphological, optical, magnetic and catalytic properties of spinel ZnFe2O4 nanoparticles.* Journal of nanoscience and nanotechnology, 2016. **16**(6): p. 5929–5943.
7. Miao, Q., et al., *Magnetic properties of N-doped graphene with high Curie temperature.* Scientific reports, 2016. **6**(1): p. 21832.
8. Patil, R., et al., *Synthesis, structural and magnetic properties of different metal ion substituted nanocrystalline zinc ferrite.* Results in Physics, 2013. **3**: p. 129–133.
9. Trukhanov, A., et al., *Correlation between the composition, structural parameters and magnetic properties of spinel-based functional nanocomposites.* Nano-Structures & Nano-Objects, 2023. **33**: p. 100941.
10. Muscas, G., et al., *Magnetic interactions versus magnetic anisotropy in spinel ferrite nanoparticles.* IEEE Magnetics Letters, 2019. **10**: p. 1–5.
11. Salih, S.J. and W.M. Mahmood, *Review on magnetic spinel ferrite (MFe2O4) nanoparticles: From synthesis to application.* Heliyon, 2023. **9**(6).
12. Xu, H., et al., *Current and future trends for spinel-type electrocatalysts in electrocatalytic oxygen evolution reaction.* Coordination Chemistry Reviews, 2023. **475**: p. 214869.
13. Liu, G., et al., *Thermodynamics and electronic structure characteristics of MFe2O4 with different spinel structures: A first-principles study.* Ceramics International, 2023. **49**(18): p. 29747–29754.
14. Flores-Lasluisa, J.X., et al., *Transition metal oxides with perovskite and spinel structures for electrochemical energy production applications.* Environmental Research, 2022. **214**: p. 113731.
15. Fesenko, O. and L. Yatsenko, *Nanophysics, nanomaterials, interface studies, and applications.* Springer Proceedings in Physics, 2017. **195**.
16. Channa, N., et al., *Nickel-substituted manganese spinel ferrite nanoparticles for high-frequency applications.* Journal of Materials Science: Materials in Electronics, 2020. **31**(2): p. 1661–1671.
17. Jouini, A., et al., *Optical properties of transition metal ion-doped MgAl2O4 spinel for laser application.* physica status solidi c, 2007. **4**(3): p. 1380–1383.
18. Gonçalves, J.M., et al., *Feasible strategies to promote the sensing performances of spinel MCo 2 O 4 (M= Ni, Fe, Mn, Cu and Zn) based electrochemical sensors: a review.* Journal of Materials Chemistry C, 2021. **9**(25): p. 7852–7887.
19. El Abboubi, M. and S.E. San, *Integration of spinel ferrite magnetic nanoparticles into organic solar cells: a review.* Materials Science and Engineering: B, 2023. **294**: p. 116512.
20. Nandwana, V. and V.P. Dravid, *Multicomponent magnetic spinels: From complexity of crystal chemistry to coupled magnetic resonance imaging (MRI).* APL Materials, 2023. **11**(5).

21. Amani, S., et al., *Synthesis and investigation of CoMnFeO4/reduced graphene oxide as ecofriendly electrode material for supercapacitor and its electrochemical performances.* Journal of Alloys and Compounds, 2023. **937**: p. 168020.
22. Maksoud, M.A., et al., *Antibacterial, antibiofilm, and photocatalytic activities of metals-substituted spinel cobalt ferrite nanoparticles.* Microbial pathogenesis, 2019. **127**: p. 144–158.
23. Kocevski, V., G. Pilania, and B.P. Uberuaga, *High-throughput investigation of the formation of double spinels.* Journal of Materials Chemistry A, 2020. **8**(48): p. 25756–25767.
24. Divya, S., et al., *Impact of Zn doping on the dielectric and magnetic properties of CoFe2O4 nanoparticles.* Ceramics International, 2022. **48**(22): p. 33208–33218.
25. Saei, J.N. and K. Asadpour-Zeynali, *Enhanced electrocatalytic activity of fluorine doped tin oxide (FTO) by trimetallic spinel ZnMnFeO4/CoMnFeO4 nanoparticles as a hydrazine electrochemical sensor.* Scientific Reports, 2023. **13**(1): p. 12188.
26. Zhang, G., A. Goldstein, and Y. Wu, *Novel transparent MgGa2O4 and Ni2+-doped MgGa2O4 ceramics.* Journal of Advanced Ceramics, 2022. **11**(3): p. 470–481.
27. Goda, M.N. and A.E.-A.A. Said, *Metal-organic frameworks derived CuMn2O4@ C for the sustainable production of methyl ethyl ketone as a promising biofuel.* Polyhedron, 2026: p. 118199.
28. Mohamed, R.M., et al., *Fabrication of np heterojunction CuMn2O4/BaZrO3 nanocomposite with boosted photocatalytic ability: Herbicides atrazine as a case study.* Journal of Alloys and Compounds, 2026: p. 186968.
29. Chen, D., et al., *Catalytic activity of supported Cu-Mn/fly ash geopolymer for the oxidative removal of toluene.* Scientific Reports, 2025. **15**(1): p. 42567.
30. Dos Santos, M., et al., *Intrinsic magnetic properties of BixCo2− xMnO4 spinels obtained by short-time etching.* Journal of magnetism and magnetic materials, 2013. **339**: p. 157–162.
31. Schwarz, K. and P. Blaha, *Solid state calculations using WIEN2k.* Computational Materials Science, 2003. **28**(2): p. 259–273.
32. Perdew, J.P., K. Burke, and M. Ernzerhof, *Generalized gradient approximation made simple.* Physical review letters, 1996. **77**(18): p. 3865.

CHAPTER I

GENERAL OVERVIEW OF SPINEL MATERIALS

CHAPTER 1 GENERAL OVERVIEW OF SPINEL MATERIALS

1.1. Introduction

Spinel-type materials occupy a prominent position in many scientific and technological fields due to their distinctive structural, magnetic, and electrical properties. Their crystalline structure, which determines the arrangement of atoms within the lattice, plays a crucial role in defining their unique physical characteristics. Spinels are particularly important within the family of ferrites, which have been widely investigated for applications in electronics, magnetism, and data storage because of their diverse magnetic behaviors, including ferrimagnetism and characteristic hysteresis cycles.

To gain a deeper understanding of these magnetic phenomena, crystal field theory is commonly employed, as it provides valuable insight into the role of 3d electrons in the magnetic dynamics of spinel compounds. In addition, the electrical properties of these materials have attracted significant interest, especially because of their potential as magnetic semiconductors. This multifunctional nature opens up promising opportunities for advanced technological applications, particularly in the rapidly developing field of spintronics.

1.2. Crystal Structure of Spinels

The general form0ula AB_2O_4 adopts a spinel crystal structure similar to that of the natural spinel MgAl2O4 [1]. This cubic structure belongs to the Fd3m space group (No. 227) and is characterized by a compact arrangement of oxygen ions forming a face-centered cubic lattice. Within this lattice, the cations are distributed between two types of interstitial sites: octahedral sites (Oh) and tetrahedral sites (Td).

This specific cation distribution results in the formation of eight structural units (or octants) of AB_2O_4 within each unit cell. These units illustrate the spatial arrangement of A^{2+} and B^{3+} cations surrounding the O^{2-} anions, highlighting the structural complexity of spinel compounds.

The primitive unit cell is rhombohedral and contains two formula units of AB_2O_4. However, since this cell is not convenient for describing the crystal structure, the smallest multiple cubic unit cell is generally used instead. This cubic cell contains 32 oxygen atoms, which define 32 B sites and 64 A sites. Among these, only 8 A sites and 16 B sites are actually occupied by cations . Consequently, the smallest cubic unit cell contains eight formula units of AB_2O_4 [2]

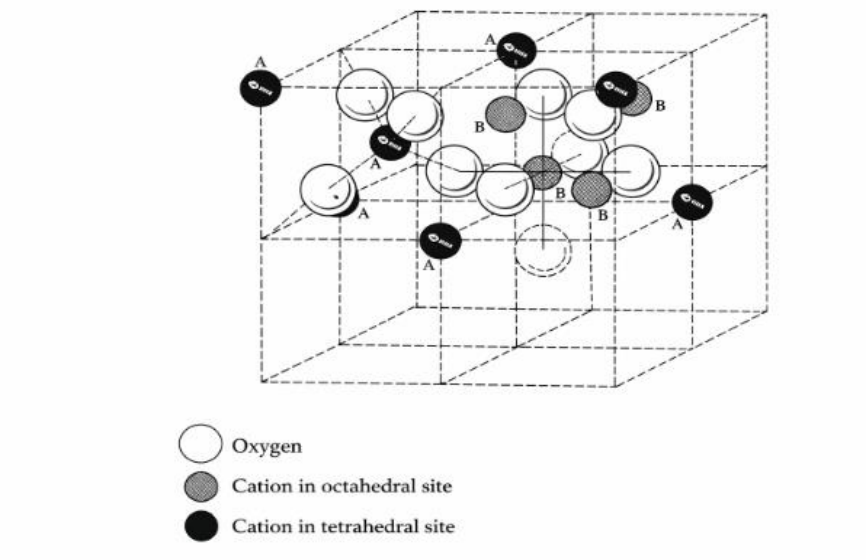

Figure 1.1 : *Unit cell of the AB_2O4 spinel structure*

To provide a detailed description of the structure, the unit cell with lattice parameter a is conventionally subdivided into eight smaller cubes, commonly referred to as octants, each characterized by an edge length of a/2. As illustrated in Figure I-1, the spatial distribution of both cations and anions can be observed within two neighboring octants. The oxygen anions adopt an identical arrangement in all octants, occupying positions that correspond to the vertices of a tetrahedron inscribed within a cube of edge a/4 [3].

The occupied A sites are located at the center of alternating octants and additionally at half of the vertices of all octants. Within the cubic unit cell, these A sites form two interpenetrating face-centered cubic (FCC) sublattices, which are displaced relative to one another by a vector of magnitude $a\sqrt{3}/4$ along the [111] crystallographic direction. The B sites, on the other hand, are also distributed in alternating octants. Similar to the oxygen ions, they are positioned at one quarter of the octant diagonal measured from four of the eight octant vertices, thereby forming a tetrahedral arrangement inscribed within a cube of edge a/4 [4].

In practice, the oxygen anions do not occupy the exact positions of a perfect FCC sublattice. Their precise locations are defined by the oxygen positional parameter u, which determines the displacement of the O^{2-} ions relative to the ideal lattice positions. This parameter corresponds to the distance between an oxygen anion and the cations located at tetrahedral (Td) sites [5]. The value of u is expressed as a fraction of the lattice parameter a. For an ideal spinel structure, u = 0.375; however, such an ideal configuration is rarely realized in practice. For the majority of known spinel compounds, the oxygen parameter typically lies within the range $0.375 \leq u \leq 0.385$ [6].

The presence of O^{2-} ions within a face-centered cubic (FCC) oxygen framework, together with the availability of both tetrahedral (Td) and octahedral (Oh) interstitial sites, allows for different possible ionic distributions among these nonequivalent crystallographic positions. Such cation arrangements are commonly described by a parameter known as the degree of inversion (λ). This parameter represents the fraction of divalent cations occupying octahedral sites. Accordingly, the general formula of a spinel structure can be expressed as follows (by convention, octahedral sites are written in brackets) [7]

$$A^{2+}_{1-2\lambda}\, B^{3+}_{2\lambda}\left[A^{2+}_{2\lambda}\;\; B^{3+}_{2-2\lambda}\right] \qquad \text{(I.1)}$$

Where **λ** denotes the degree of inversion.

When **λ = 0**, the compound is referred to as a normal spinel, and the cation distribution can be written as: A $[B_2]$ O_4 For $\lambda \approx 0.33$, the structure is considered statistically disordered or partially inverse (mixed spinel). When $\lambda = 0.5$, the structure corresponds to an inverse spinel, which can be represented as: B [AB] O_4

Thus, spinel compounds can generally be classified into two main categories depending on the cation distribution: normal spinels and inverse spinels. In a normal spinel structure, the A^{2+} cations exclusively occupy the tetrahedral (T_d) sites, while the B^{3+} cations are located at the octahedral (O_h) sites. In contrast, in an inverse spinel structure, half of the B^{3+} cations occupy the tetrahedral sites, whereas the A^{2+} cations together with the remaining half of the B^{3+} cations are distributed over the octahedral sites.

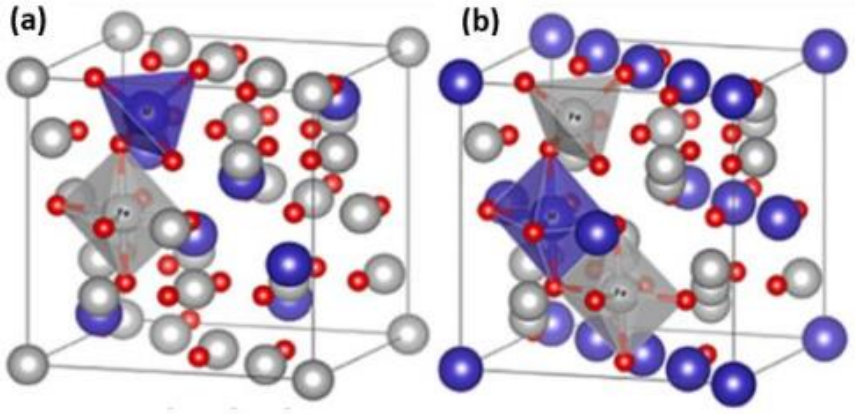

Figure 1- 2*(a) Normal spinel structure, (b) Inverse spinel structure[8]*

Double spinel structure: Defined by the chemical formula ABB′O_4, the double spinel structure is characterized by an ordered arrangement of divalent and trivalent cations, combining features of both normal and inverse spinels. This implies a distinct spatial separation of divalent and trivalent cations; however, the distribution does not strictly correspond to either a purely normal or purely inverse spinel configuration. In this structure,

A^{2+} ions occupy the octahedral sites of a normal spinel sublattice, whereas B^{3+} and B'^{3+} ions occupy the octahedral and tetrahedral sites, respectively, within an inverse spinel sublattice [9, 10]

According to the work of Pilania *et al.*, such cation mixing across different sublattices can occur at relatively low temperatures for specific spinel compositions, making the synthesis of double spinel structures particularly challenging. Their findings demonstrate not only the theoretical feasibility but also the experimental realization of these compounds, thereby opening new avenues for the design of spinel-based materials with tailored functionalities.

Double spinel structures thus constitute an emerging class of materials exhibiting a wide range of distinctive properties compared to conventional normal and inverse spinels, primarily due to their unique cation arrangements. For instance, they may display enhanced ionic conductivity, unconventional magnetic behavior, and improved resistance to degradation.

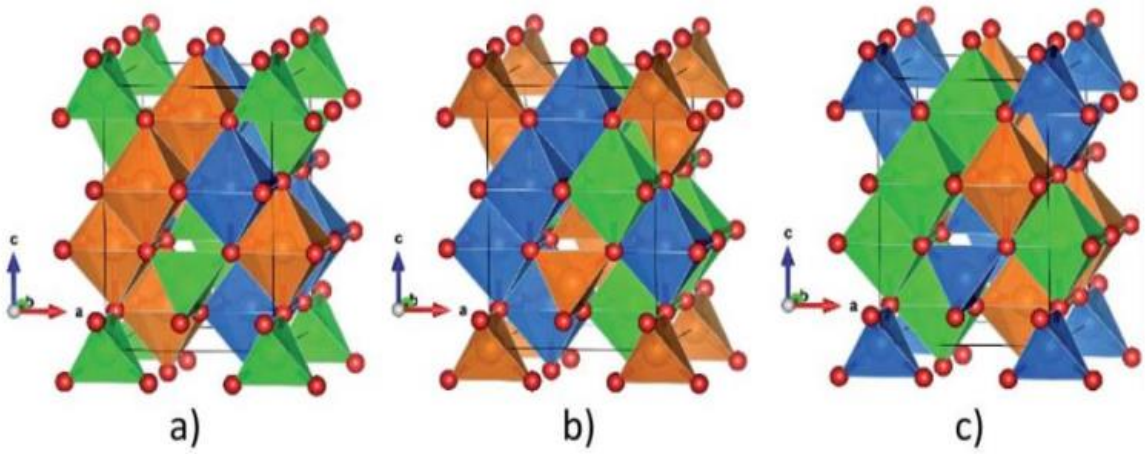

Figure 1-3: *(a) Inverse double spinel 1 [B'ABO₄], (b) Normal double spinel [ABB'O₄], and (c) Inverse double spinel [(B)AB'O₄]. The A, B, and B' cations are represented in orange, blue, and green, respectively, while the oxygen atoms are shown in red.*

1.3. Spinel-Type Ferrites

Spinel ferrites, commonly referred to simply as ferrites, are primarily composed of trivalent iron and oxygen. Their general chemical formula is MFe_2O_4, where M denotes a divalent metal cation, while iron is present in its trivalent state [11]. The ferrites most relevant for practical applications are often complex compositions in which M consists of a combination of divalent ions such as Mn^{2+}, Ni^{2+}, Zn^{2+}, Fe^{2+}, Co^{2+}, and Cu^{2+}.

CHAPTER 1 GENERAL OVERVIEW OF SPINEL MATERIALS

Ferrites are classified as “soft” magnetic materials due to the absence of a preferred direction of magnetization [12]. This means that their magnetization direction can be easily altered under the influence of an external magnetic field [13]. The magnetic properties of ferrites depend not only on the nature of the metal ions occupying the interstitial sites but also on their distribution within the crystal lattice. These characteristics make ferrites highly suitable for a wide range of applications, including magnetic storage media, microwave devices, and magnetic sensors [14, 15].

1.4. Magnetic Properties of Spinels

1.4.1. Types of Magnetism

I.4.1.a. Ferromagnetism

Ferromagnetic materials are characterized by spontaneous magnetization, in which the magnetic moments of atoms or ions align parallel to one another, even in the absence of an external magnetic field. This alignment results in a permanent net magnetization. The Curie temperature is the critical temperature above which the material loses its permanent magnetization and becomes paramagnetic. At this temperature, the magnetic moments become randomly oriented due to thermal agitation.

I.4.1.b Antiferromagnetism

Antiferromagnetic materials exhibit an antiparallel coupling of the magnetic moments of atoms or ions. Below the Néel temperature, these moments align in opposite directions, effectively canceling out the net magnetization of the material. The magnetic susceptibility of antiferromagnetic materials is relatively low, and their magnetic response differs from that of ferromagnetic materials. The Néel temperature is the temperature above which the material loses its antiparallel magnetic order and becomes paramagnetic. Beyond this temperature, thermal agitation causes a random orientation of the magnetic moments.

I.4.1.c Ferrimagnetism

Ferrimagnetic materials are distinguished by an antiparallel alignment of magnetic moments; however, unlike antiferromagnetic materials, these moments do not completely cancel each other. This is due to the difference in magnitude between opposing magnetic moments, resulting in a net magnetization [16]. This type of magnetic ordering is typical of ferrites, which are widely used in various technological applications. Similar to ferromagnetic materials, ferrimagnetic materials become paramagnetic above the Curie temperature. However, they may also exhibit a compensation temperature at which the net magnetization becomes zero before reaching the Curie temperature.

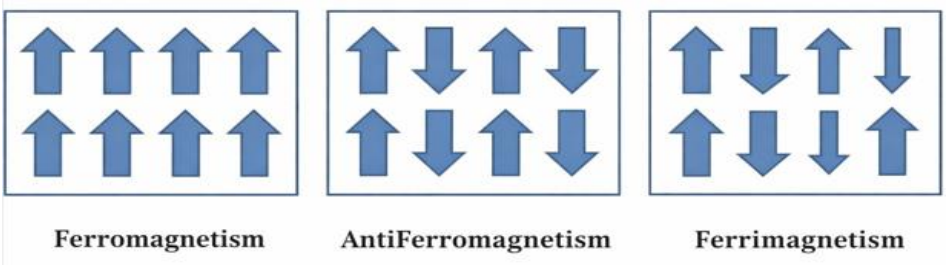

Figure I-4 Different magnetic ordering in materials: ferromagnetism, antiferromagnetism, and ferrimagnetism.

1.4.2. Magnetic Hysteresis Cycle

The magnetization of a ferrimagnetic material under the application of a magnetic field *H* follows a magnetic hysteresis cycle (Figure I-5).

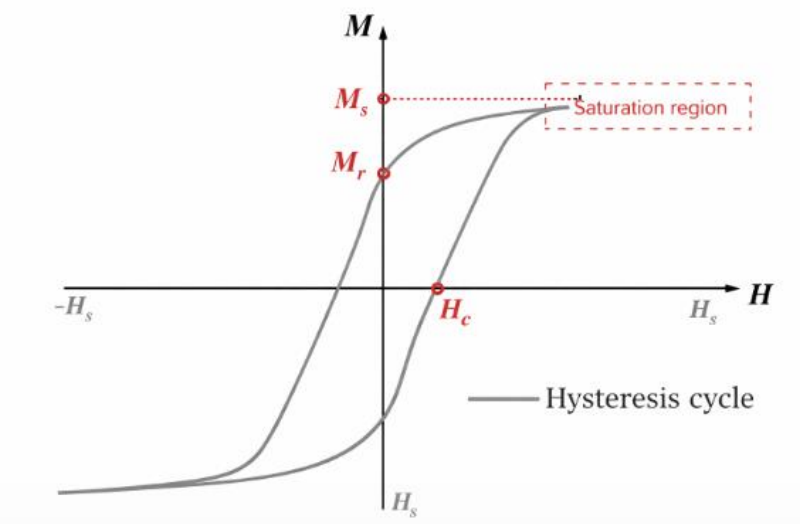

Figure 1-5: *Magnetic Hysteresis Cycle*

When the applied magnetic field is zero, a residual magnetization M_r remains, called remanent magnetization. To reduce and eliminate this magnetization, the direction of the applied field must be reversed until reaching a value H_c known as the coercive field. Both the coercive field and the remanent magnetization vary with temperature. Beyond a certain temperature, called the Curie temperature, the hysteresis loop closes, and the material becomes paramagnetic [17].

The hysteresis cycle for a ferrimagnetic material is generally similar in shape to that of a ferromagnetic material, but the values of M_r and H_c can differ depending on the specific composition and structure of the material. The loop width may vary, reflecting differences in the internal magnetic interactions.

Magnetic domains: The magnetic properties of ferrite particles also depend, at equal composition, on the size of the crystallites. When crystallites have dimensions larger than

approximately one micrometer, they consist of multiple magnetic domains separated by Bloch walls. Each domain possesses a permanent magnetic moment due to the crystallographic orientation of the structure. Magnetization reversal occurs through the displacement of these walls under the action of a relatively weak applied field [18].

For sizes below approximately 1 µm, the grains are single-domain. Each particle then exhibits a permanent magnetic moment whose direction is fixed by the easy axis of magnetization. In this case, magnetization occurs through the rotation of the magnetic moments of the ions, and the coercivity reaches its maximum value.

1.4.3. Ferrimagnetism in Ferrites

The magnetic properties of spinel ferrites are interpreted within Néel's ferrimagnetism theory [19]. This theory is based on the existence of magnetic order resulting from spin–spin interactions between metal cations. Néel proposed that two magnetic sublattices exist, with moments that are antiparallel but unequal in magnitude. These two sublattices correspond to the two crystallographic sites, T_d and O_h in the spinel structure.

Néel further proposed that exchange forces act between the metal cations located at T_d and O_h sites via the oxygen ions. At high doping levels, the interaction between octahedral sites (O_h) becomes predominant, and the compounds become antiferromagnetic. In such materials, the atomic coupling is antiparallel with equal magnitude, resulting in a net magnetic moment of zero; thus, the susceptibility is very small and positive. These couplings are destroyed by thermal agitation at a critical temperature called the Néel temperature. Beyond this temperature, antiferromagnetic materials become paramagnetic.

1.5. Crystal Field Theory

Crystal Field Theory (CFT) is a crucial model for understanding the structure and properties of coordination complexes, fascinating compounds formed by the association of a central metal ion (cation) with neutral or negatively charged molecules or ions (ligands) [20]. The metal ion is surrounded by ligands arranged symmetrically around it. This geometry, reminiscent of a crystal lattice, gives the theory its name.

According to CFT, the ligands create an electric field that affects the energy orbitals of the metal ion's electrons, destabilizing some and stabilizing others in a differential manner [21].

1.5.1. 3d Elements

Transition elements have an incomplete 3d electron shell, which leads to the presence of localized magnetic moments (Figure I-6). The 3d electrons of the magnetic ions do not

form a separate band due to their limited overlap. However, they can influence the electronic properties of the bands through hybridization with the p states of the valence band.

The 3d shell splits into a fully occupied 3d↑ level and an empty or partially filled 3d↓ level, depending on the type of transition ion (Mn, Fe, Co, …).

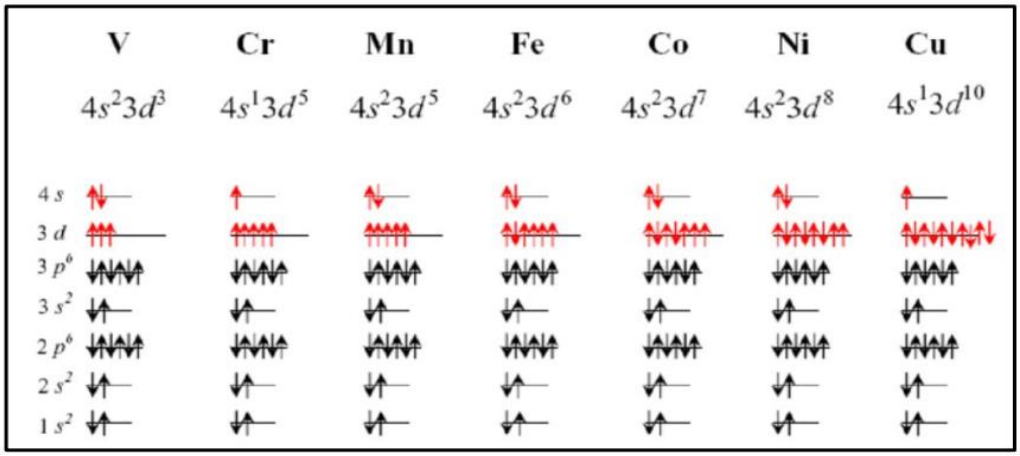

0-6: *Electronic configuration of the 3d and 4s states of transition metals[22].*

1.5.2. Degeneracy of d Orbitals

The crystal field has a significant effect on the d orbitals of a metal ion, destabilizing them unequ0ally and removing their degeneracy. The magnitude of this splitting depends on the geometry of the 0crystal field, which is determined by the arrangement of ligands around the metal ion.

- **Octahedral field:** In an octahedral crystal field, six ligands surround the central metal ion, forming an octahedron. The ligands are positioned along the x, y, and z axes, creating a non-uniform electric field that destabilizes the d orbitals pointing toward the ligands (antibonding orbitals) and stabilizes those located between the ligands (bonding orbitals). The d orbitals split into two groups:

- **t_{2g} orbitals:** $3d_{xy}$, $3d_{yz}$, $3d_{zx}$ (stabilized).
- **e_g orbitals:** dz^2, $d_{x^2-y^2}$ (destabilized).

The energy difference between the t_{2g} and e_g orbitals is called the crystal field splitting parameter (Δ_o).

- **(b) Tetrahedral field:** In a tetrahedral crystal field, four ligands surround the central metal ion, forming a tetrahedron. The ligands are positioned at equal angles from one another, creating an electric field that is less non-uniform than in an octahedral field. The d orbitals split into two groups:

- **t_2 orbitals:** (stabilized).
- **e orbitals:** (destabilized).

The energy difference between the t_2 and e orbitals is smaller than Δ_0 in an octahedral field.

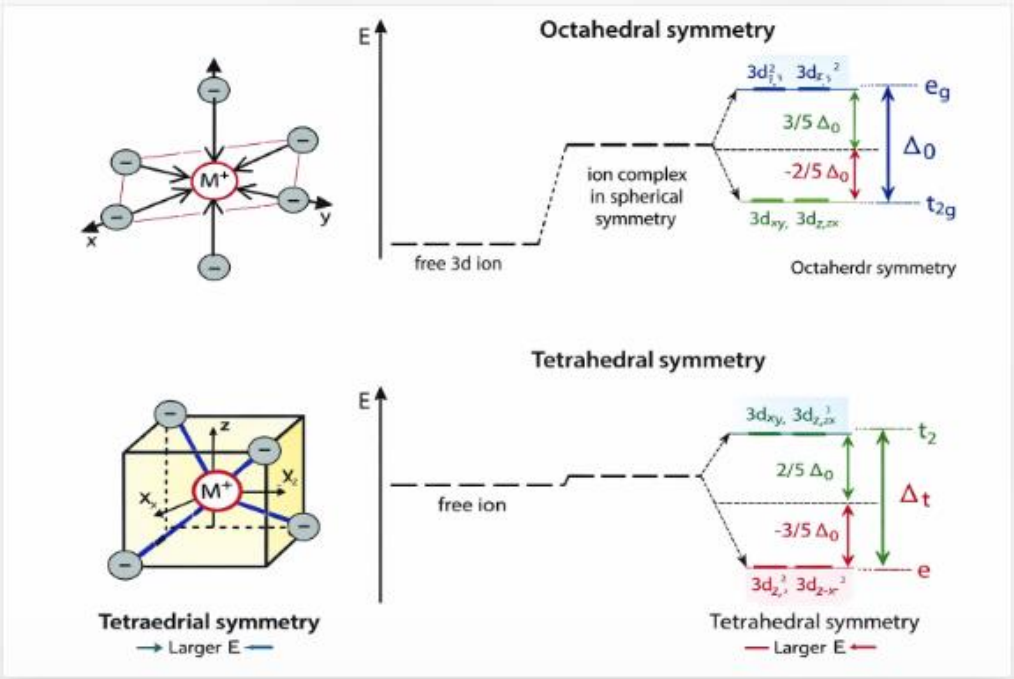

Figure 0-7: *Influence of the crystal field on the energy levels of d orbitals, (a) octahedral field, (b) tetrahedral field.*

The lifting of degeneracy of d orbitals induced by the crystal field has major implications for the properties and behavior of complexes in various physical contexts. The color of metal complexes is directly influenced by this splitting. Electronic transitions between d orbitals, caused by field, are responsible for the absorption or emission of visible light, giving the complex its characteristic color. This property is essential in spectroscopy and in the analysis of chemical compounds [23]

Furthermore, the lifting of degeneracy has a significant impact on the magnetic properties of complexes. The presence of unpaired electrons in the d orbitals, resulting from this interaction, gives rise to magnetic behavior. The specific distribution of these electrons determines the overall magnetic moment of the complex, which is crucial for understanding its magnetic characteristics.

1.6. Electrical Properties

1.6.1. Conduction in Spinel Ferrites

The Verwey mechanism, proposed by E.J.W. Verwey in the 1950s, explains electronic conduction at room temperature in spinel ferrites. According to this model, conduction does not arise from the movement of free electrons but rather from polaron hopping between cations of the same element with oxidation states differing by one unit and occupying equivalent crystallographic sites [24].

In this framework, conduction occurs via polaron hopping. A polaron is a quasiparticle formed by an electron coupled with a local distortion of the crystal lattice [25]. This model specifically excludes electron transfer between the two crystallographic sublattices of the spinel structure, namely tetrahedral (T_d) and octahedral (O_h) sites. It favors hopping between octahedral sites (O_h), considering intersite distances to determine the most energetically favorable electron transfer.

The intersite distances in spinel ferrites are :

$$d_{OhOh} = a\frac{\sqrt{2}}{4} \; et \; d_{TdTd} = a\frac{\sqrt{3}}{4} \qquad \text{(I.2)}$$

Electron hopping between octahedral sites (O_h) requires the lowest energy, as this distance is the shortest. Hopping between octahedral and tetrahedral sites, or between tetrahedral sites, is less likely due to the higher energy required for longer distances.

Electrical conductivity is strongly influenced by the distribution of cations in octahedral and tetrahedral sites. The Verwey mechanism also explains the relatively high electrical resistivity of spinel ferrites compared to metals.

1.6.2. Negative Temperature Coefficient (NTC) Behavior in Spinel Ferrites

NTC (Negative Temperature Coefficient) spinel ferrites exhibit distinctive properties that make them suitable for various technological applications [26]. Their temperature coefficient (α) is generally negative, meaning that resistivity decreases as temperature increases, making them highly sensitive to thermal variations.

Moreover, these ferrites have high values of the sensitivity factor (B), indicating strong variation of resistivity over a given temperature range, which allows precise temperature measurement and control.

In addition to their exceptional sensitivity, NTC spinel ferrites are chemically and mechanically stable, making them suitable for use in harsh environments. This combination of thermal sensitivity and robustness gives NTC spinel ferrites a crucial role in many industrial and technological applications [27, 28].

1.6.3. Magnetic Semiconductors

Magnetic semiconductors are a fascinating class of materials that exhibit both semiconducting and magnetic properties [29]. This unique combination allows control of both electrical and magnetic properties, enabling revolutionary applications in spintronics and magneto-electronics.

A key concept in magnetic semiconductors is the spin–charge interaction. Conduction electrons carry both charge and a magnetic moment due to spin. Consequently, the magnetic state of the system can influence conduction, and vice versa.

The Goodenough model explains how magnetic ordering affects electron conduction in these materials [30]. According to this model, electron transfer from a donor to an acceptor site is more likely when the 3d electron spins of the donor and acceptor cations are parallel.

The transfer energy depends on the factor $cos(\theta/2)$, where θ is the angle between the 3d electron spins at two neighboring conduction sites. Electron hopping is easier when spins are aligned ($\theta = 0$) than when antiparallel ($\theta = \pi$). Ferromagnetic semiconductors, with aligned spins, have relatively low resistivity, while antiferromagnetic semiconductors, with antiparallel spins, show higher resistivity due to increased carrier localization.

1.7. Applications and Technology

Spinel ferrites exhibit remarkable magnetic and dielectric properties, making them attractive for various technological applications [31].

1.7.1. Telecommunications

Ferrites are essential in telecommunications, particularly in microwave filters, circulators, and isolators [32]. In microwave filters, ferrites are integrated into resonators or transmission lines where their magnetic permeability varies with frequency, allowing bandwidth control and improved signal selectivity. An external magnetic field can adjust their magnetic properties, enabling dynamic tuning of the filters.

In circulators—passive devices that direct electromagnetic signals through a network of ports—ferrites exploit the gyromagnetic effect. A static magnetic field induces precession of electron magnetic moments, causing rotation of electromagnetic waves. This rotation directs signals unidirectionally, avoiding unwanted feedback.

Isolators protect sensitive components from signal reflections by allowing signals to pass in one direction only. Using the gyromagnetic properties of ferrites, an applied magnetic field induces non-reciprocal wave rotati0on, permitting waves to pass in one direction with

minimal loss while strongly attenuating reflected waves. This prevents interference in communication systems.

1.7.2. Radars and Electronic Defense

Ferrites enhance radar and electronic defense systems by increasing sensitivity and reducing interference. Their ability to absorb electromagnetic waves enables efficient wave absorbers, improving radar signal clarity and precision [33].

They can also be used for signal jamming. Exploiting the gyromagnetic effect, ferrites allow precise manipulation of electromagnetic signals under a static magnetic field, enhancing jamming efficiency [34].

1.7.3. Consumer Electronics

Miniaturized, low-loss ferrites are promising for consumer electronics such as smartphones, tablets, and laptops. Microwave filters and antennas made from ferrites improve connectivity and performance. By reducing interference and enhancing signal transmission, ferrites contribute to better reception and more reliable wireless communication. Their integration enables more compact devices without compromising performance [35].

1.7.4. Electric and Hybrid Vehicles

Ferrites can be used in power converters and filters for electric and hybrid vehicles. These components efficiently convert battery energy into usable motor energy, optimizing performance. Ferrites reduce electromagnetic interference, improving onboard electronic system reliability and safety. Their ability to handle high currents and minimize energy loss makes them essential for vehicle efficiency and durability [36].

1.7.5. Renewable Energy

Ferrites are used in power converters and filters for renewable energy systems, such as wind turbines and solar panels. These components efficiently convert energy from renewable sources into electricity for the grid. Their high magnetic permeability and low energy loss optimize energy conversion and reduce electromagnetic interference, enhancing overall system efficiency [37].

1.7.6. Medical Imaging

In medical imaging, ferrites' magnetic properties make them useful for MRI. Ferrite nanoparticles serve as contrast agents, improving MRI resolution and sensitivity. Their magnetic moments create local magnetic field variations, enhancing image contrast and enabling more accurate diagnoses [38].

1.7.7. Magnetic Hyperthermia

Ferrites are also used in magnetic hyperthermia cancer treatment, where alternating magnetic fields heat tumors. Injected ferrite nanoparticles 0heat under an external magnetic field, raising local temperature and selectively destroying cancer cells [39].

1.7.8. Catalysis

Ferrites' catalytic properties make them useful for various chemical reactions. They serve as catalysts for pollutant degradation, chemical production, and energy conversion. Their crystal structure and chemical reactivity facilitate these processes [40, 41].

Research on ferrites continues to evolve, with new applications constantly emerging. Their unique properties make them promising for a wide range of technological applications, advancing various fields and improving daily life.

References

1. Tropf, W.J. and M.E. Thomas, *Magnesium aluminum spinel (MgAl2O4)*, in *Handbook of optical constants of solids*. 1997, Elsevier. p. 883–894a.
2. Szotek, Z., et al., *Electronic structures of normal and inverse spinel ferrites from first principles.* Physical Review B—Condensed Matter and Materials Physics, 2006. **74**(17): p. 174431.
3. Taffa, D.H., et al., *Photoelectrochemical and theoretical investigations of spinel type ferrites (M x Fe3− x O4) for water splitting: a mini-review.* Journal of Photonics for Energy, 2017. **7**(1): p. 012009–012009.
4. Hosseini, S., *Structural, electronic and optical properties of spinel MgAl2O4 oxide.* physica status solidi (b), 2008. **245**(12): p. 2800–2807.
5. Hill, R.J., J.R. Craig, and G. Gibbs, *Systematics of the spinel structure type.* Physics and chemistry of minerals, 1979. **4**(4): p. 317–339.
6. Sickafus, K.E., J.M. Wills, and N.W. Grimes, *Structure of spinel.* Journal of the American Ceramic Society, 1999. **82**(12): p. 3279–3292.
7. Bhattacharya, J. and C. Wolverton, *Relative stability of normal vs. inverse spinel for 3d transition metal oxides as lithium intercalation cathodes.* Physical Chemistry Chemical Physics, 2013. **15**(17): p. 6486–6498.
8. Mapossa, A.B., et al., *Removal of organic dyes from water and wastewater using magnetic ferrite-based titanium oxide and zinc oxide nanocomposites: a review.* Catalysts, 2021. **11**(12): p. 1543.
9. Kocevski, V., G. Pilania, and B.P. Uberuaga, *High-throughput investigation of the formation of double spinels.* Journal of Materials Chemistry A, 2020. **8**(48): p. 25756–25767.
10. Pilania, G., et al., *Prediction of structure and cation ordering in an ordered normal-inverse double spinel.* Communications Materials, 2020. **1**(1): p. 84.
11. Brabers, V., *Progress in spinel ferrite research.* Handbook of magnetic materials, 1995. **8**: p. 189–324.
12. Sundahl Jr, R. and Y. Kim, *Soft Magnetic Ferrites*, in *Concise Encyclopedia of Advanced Ceramic Materials*. 1991, Elsevier. p. 440–445.
13. Zarai, W., et al., *Effect of Calcination Temperature on Structural and Optical Properties of Mg0. 6Co0. 4FeAlO4 Spinel Ferrites for Optoelectronic Applications and Non-volatile Organic Memories.* Journal of Inorganic and Organometallic Polymers and Materials, 2026. **36**(1): p. 243–258.
14. Narang, S.B. and K. Pubby, *Nickel spinel ferrites: a review.* Journal of Magnetism and Magnetic Materials, 2021. **519**: p. 167163.
15. Dippong, T., E.A. Levei, and O. Cadar, *Recent advances in synthesis and applications of MFe2O4 (M= Co, Cu, Mn, Ni, Zn) nanoparticles.* Nanomaterials, 2021. **11**(6): p. 1560.
16. Néel, L., *Antiferromagnetism and ferrimagnetism.* Proceedings of the Physical Society. Section A, 1952. **65**(11): p. 869–885.
17. Jiles, D.C. and D.L. Atherton, *Theory of ferromagnetic hysteresis.* Journal of magnetism and magnetic materials, 1986. **61**(1-2): p. 48–60.
18. Marrows, C., *Spin-polarised currents and magnetic domain walls.* Advances in Physics, 2005. **54**(8): p. 585–713.
19. Smart, J.S., *The Néel theory of ferrimagnetism.* American Journal of Physics, 1955. **23**(6): p. 356–370.

20. Burdett, J.K., G.D. Price, and S.L. Price, *Role of the crystal-field theory in determining the structures of spinels.* Journal of the american chemical society, 1982. **104**(1): p. 92–95.
21. Ali, S., et al., *Crystal field splitting, half metallic ferromagnetism, structural, mechanical and magneto-electronic properties of spinels type structure compounds MgX2O4 (X= Fe and Co) for spintronic applications.* The European Physical Journal Plus, 2021. **136**(7): p. 1–15.
22. Liu, C., F. Yun, and H. Morkoc, *Ferromagnetism of ZnO and GaN: a review.* Journal of Materials Science: Materials in Electronics, 2005. **16**(9): p. 555–597.
23. Andreozzi, G.B., et al., *Color mechanisms in spinel: A multi-analytical investigation of natural crystals with a wide range of coloration.* Physics and Chemistry of Minerals, 2019. **46**(4): p. 343–360.
24. Jackson, M.J. and B. Moskowitz, *On the distribution of Verwey transition temperatures in natural magnetites.* Geophysical Journal International, 2021. **224**(2): p. 1314–1325.
25. Goodenough, J.B., *The Verwey transition revisited*, in *Mixed-Valence Compounds: Theory and Applications in Chemistry, Physics, Geology, and Biology*. 1980, Springer. p. 413–425.
26. Acharya, N. and R. Sagar, *Structure and electrical properties characterization of NiMn2O4 NTC ceramics.* Inorganic Chemistry Communications, 2021. **132**: p. 108856.
27. Jagtap, S., et al., *Preparation, characterization and electrical properties of spinel-type environment friendly thick film NTC thermistors.* Journal of the European Ceramic Society, 2008. **28**(13): p. 2501–2507.
28. Reimann, T. and J. Töpfer, *Low-temperature sintered Ni–Zn–Co–Mn–O spinel oxide ceramics for multilayer NTC thermistors.* Journal of Materials Science: Materials in Electronics, 2021. **32**(8): p. 10761–10768.
29. Böer, K.W. and U.W. Pohl, *Magnetic Semiconductors*, in *Semiconductor Physics*. 2023, Springer. p. 319–365.
30. Goodenough, J.B., *Magnetic Semiconductors Intrigue Both Scientists and Engineers*. 1970, American Institute of Physics.
31. Dolgopolova, E.A., et al., *Strong Purcell enhancement at telecom wavelengths afforded by spinel Fe 3 O 4 nanocrystals with size-tunable plasmonic properties.* Nanoscale Horizons, 2022. **7**(3): p. 267–275.
32. Kumar, S. and R.R. Singh, *Ferrite nanoparticles for telecommunication application*, in *Engineered ferrites and their applications*. 2023, Springer. p. 95–112.
33. Kaur, M. and S. Bahel, *Frequency and thickness dependent absorption analysis of pure and substituted Zn-Co spinel ferrites for radar applications.* Materials Today: Proceedings, 2024.
34. Xiang, N., et al., *The in situ preparation of Ni–Zn ferrite intercalated expanded graphite via thermal treatment for improved radar attenuation property.* Molecules, 2023. **28**(10): p. 4128.
35. Miligy, A.F. *Analysis and Design of Improved Guided Wave Structure Using Matching Network/Magnetized Material and Circular Spiral-Spiral Wraparound Metamaterial Array for X-Band Radar Applications*. in *2023 International Telecommunications Conference (ITC-Egypt)*. 2023. IEEE.
36. Gonçalves, J.M., et al., *Multifunctional spinel MnCo 2 O 4 based materials for energy storage and conversion: a review on emerging trends, recent developments*

and future perspectives. Journal of Materials Chemistry A, 2021. **9**(6): p. 3095–3124.
37. Park, M.-S., et al., *Porous nanoarchitectures of spinel-type transition metal oxides for electrochemical energy storage systems.* Physical Chemistry Chemical Physics, 2015. **17**(46): p. 30963–30977.
38. Amiri, M., M. Salavati-Niasari, and A. Akbari, *Magnetic nanocarriers: evolution of spinel ferrites for medical applications.* Advances in colloid and interface science, 2019. **265**: p. 29–44.
39. Włodarczyk, A., et al., *Magnetite nanoparticles in magnetic hyperthermia and cancer therapies: Challenges and perspectives.* Nanomaterials, 2022. **12**(11): p. 1807.
40. Bernaoui, C.R., et al., *Synthesis and characterization of NiFe2O4 nanoparticles as reusable magnetic nanocatalyst for organic dyes catalytic reduction: study of the counter anion effect.* Materials Chemistry and Physics, 2022. **292**: p. 126793.
41. Iyyappan, J., et al., *Critical review on wastewater treatment using photo catalytic advanced oxidation process: Role of photocatalytic materials, reactor design and kinetics.* Case Studies in Chemical and Environmental Engineering, 2024. **9**: p. 100599.

CHAPTER II

DENSITY FUNCTIONAL THEORY (DFT)

CHAPTER 1I DENSITY FUNCTIONAL THEORY (DFT)

2.1. Introduction

Density Functional Theory (DFT) is one of the most widely used and powerful quantum mechanical approaches for investigating the properties of matter. As a method grounded in quantum mechanics, DFT aims to describe the behavior of many-body systems by solving the Schrödinger equation and determining the ground state of the system.

The central idea of DFT is to represent a complex interacting system of particles in terms of its electron density rather than its many-body wave function. This is particularly significant because it reduces the complexity of the problem from 3N degrees of freedom for an N-particle system to only three spatial variables, making calculations far more tractable.

The origins of DFT can be traced back to the pioneering work of Thomas [1] and Fermi in the early 1930s[2]. Their contributions were later refined and extended by Hartree[3] , Dirac[4], Fock[5], and Slater. However, a rigorous theoretical foundation was not established until the seminal work of Hohenberg, Kohn, and Sham nearly four decades later, which provided the formal framework of modern DFT.

Today, DFT is extensively used to compute a wide range of physical and chemical properties, including equilibrium geometries, electronic structures, optical properties, activation energies, and reaction energies.

In this chapter, we will explore the fundamental principles underlying Density Functional Theory, review its historical development, and introduce the key concepts essential for its application.

2.2. Many-body system:

The behavior of a quantum many-body system is governed by the Hamiltonian operator, denoted as $\widehat{H}$, which encapsulates the total energy of the system, including both kinetic and potential contributions.

If $|\Psi\rangle$ represents the quantum state of the system in an abstract Hilbert space, its time evolution is described by the time-dependent Schrödinger equation:

$$i\hbar \frac{\partial \Psi}{\partial t} = \widehat{\mathrm{H}}\Psi \qquad \text{(II.1)}$$

Stationary states with well-defined energies, particularly the ground state of the system, are obtained as solutions of the time-independent Schrödinger equation, expressed as the following eigenvalue problem:

$$\widehat{\mathrm{H}}|\Psi\rangle = \mathrm{E}|\Psi\rangle \quad , \langle\Psi|\Psi\rangle = 1 \qquad \text{(II.2)}$$

Alternatively, these states can be determined through the variational principle, where the energy functional is minimized:

$$\frac{\langle\Psi|\hat{H}|\Psi\rangle}{\langle\Psi|\Psi\rangle} \rightrightarrows \ stationary \tag{II.3}$$

In this work, we consider a system composed of *N* electrons and *M* nuclei, evolving under the influence of an external field and interacting via pairwise Coulomb interactions. The total wave function of the system depends on both electronic and nuclear coordinates and can be written as:

$$\psi = \psi(\vec{r}_1, \vec{r}_2, \dots \vec{r}_N; \vec{R}_1, \vec{R}_2, \dots, \vec{R}_M) \tag{II.4}$$

And the Hamiltonian consists of:

$$\hat{H} = \hat{T}_N + \hat{T}_e + \hat{V}_{N-N} + \hat{V}_{N-e} + \hat{V}_{e-e} \tag{II.5}$$

Where:

$\hat{T}_N = -\sum_{I=1}^{M} \frac{\hbar^2}{2M_I} \nabla_I{}^2$: Thekinetic energy of nuclei

$\hat{T}_e = -\sum_{i=1}^{N} \frac{\hbar^2}{2m_e} \nabla_i{}^2$:Thekinetic energy of electrons

$\hat{V}_{N-N} = \frac{1}{2}\sum_{I\neq J} \frac{e^2}{4\pi\varepsilon_0} \frac{Z_I Z_J}{|\vec{R}_I - \vec{R}_J|}$:The potential energy of nucleus-nucleus coulomb interaction

$\hat{V}_{N-e} = \frac{1}{2}\sum_{i,J} \frac{e^2}{4\pi\varepsilon_0} \frac{Z_I}{|\vec{r}_i - \vec{R}_J|}$:Potential energy of nucleus-electron coulomb interaction

$\hat{V}_{e-e} = \frac{1}{2}\sum_{i\neq j} \frac{e^2}{4\pi\varepsilon_0} \frac{1}{|\vec{r}_i - \vec{r_j}|}$:Potential energy of electron-electron coulomb interaction

The wave function contains, in principle, all the information describing a given quantum system [6]. For simple systems such as the hydrogen atom, the Schrödinger equation can be solved exactly, leading to analytical solutions. However, for systems involving many interacting particles (so-called N-body systems), obtaining exact solutions becomes extremely difficult. The complexity arises from the large number of degrees of freedom and the interactions between particles. Consequently, it is necessary to employ simplified models and approximation methods in order to make the problem tractable and to capture the essential physical properties of the system.

2.2.1. Born-Oppenheimer approximation:

In 1927, Born and Oppenheimer introduced the well-known Born–Oppenheimer approximation [7], which provides a fundamental simplification in the study of quantum systems. This approximation is based on the large mass difference between nuclei and electrons; for instance, a proton is approximately 1836 times heavier than an electron. As a result, nuclei move much more slowly than electrons.

This disparity in mass allows for the separation of electronic and nuclear motions, an approach often referred to as the adiabatic approximation. Within this framework, electrons are treated as moving in the static potential created by fixed nuclei. Consequently, when solving the electronic problem, the nuclear positions are considered as parameters rather than dynamical variables.

Under the Born–Oppenheimer approximation, the electronic Hamiltonian can be written as:

$$.\hat{H}_e = \hat{T}_e + \hat{V}_{N-e} + \hat{V}_{e-e} \quad \text{(II.6)}$$

Within the Born–Oppenheimer framework, the total wave function of the system can be factorized into a nuclear and an electronic part:

$$\psi(\vec{R}_I, \vec{r}_i) = \varphi_N(\vec{R}_I)\psi_e(\vec{R}_I, \vec{r}_i) \quad \text{(II.7)}$$

where$\varphi_N(\vec{R}_I)$ describes he nuclear wavefunction, and $\psi_e(\vec{R}_I, \vec{r}_i)$ represents the electronic wavefunction, which depends parametrically on the nuclear positions.

Within this approximation, the Schrödinger equation for the electronic subsystem is written as:

$$\hat{H}_e\psi_e = E_e\psi_e \quad \text{(II.8)}$$

This approximation simplifies the problem, but it does not completely resolve it. For a system containing N electrons, one must still account for 3N spatial coordinates as well as N spin variables.

2.2.2. Hartree approximation:

The difficulty in solving equation (II.6) arises from electron–electron interactions, which prevent the separation of the equation into N independent electronic equations. In the Hartree approximation [3], electrons are treated as independent particles, each moving in an average field generated by the nuclei and the other electrons.

The Hamiltonian can be written:

$$\hat{H}_e = \sum_i h_i \quad \text{(II.9)}$$

Where$h_i$is : the mono electronic hamiltonian.

$$h_i = -\frac{\hbar^2}{2m_e}\nabla_i{}^2 + \hat{V}_{ext}(\vec{r}) + \hat{V}_i(\vec{r}) \quad \text{(II.10)}$$

With$\hat{V}_i(\vec{r}) = \int \frac{\rho(\vec{r}\prime)}{|\vec{r}-\vec{r}\prime|} d^3\vec{r}'$: the Hartree potential, $\hat{V}_{ext}(\vec{r})$:the Coulomb interaction of the electron with all the nuclei of the system. The electronic wave function of this Hamiltonian is a product of mono-electronic functions (Hartree Product (HP)

$$\psi_e(\vec{r}_1, \vec{r}_2, \ldots\ldots, \overrightarrow{r_N}) = \phi_1(\vec{r}_1) \ldots\ldots \phi_N(\vec{r}_N) \quad \text{(II.11)}$$

In this case, each of these mono-electronic wave function is then a solution of the Schrödinger equation to a particle which is written in the form:

$$h_i(\vec{r})\phi_i(\vec{r}) = \varepsilon_i\phi_i(\vec{r}) \quad \text{(II.12)}$$

The wave function given by equation (II.11) is not yet complete, as it does not satisfy the Pauli exclusion principle. This principle states that electrons, being fermions, require the total wave function to change sign upon exchanging any two particles. Consequently, no two electrons can occupy the same quantum state [8]. Therefore, the correct electronic wave function must be antisymmetric with respect to the exchange of two electrons:

$$\psi_e(\vec{r}_1, \vec{r}_2 \ldots \vec{r}_i, \vec{r}_j \ldots \vec{r}_N) = -\psi_e(\vec{r}_1, \vec{r}_2 \ldots \vec{r}_j, \vec{r}_i \ldots \vec{r}_N) \quad \text{(II.13)}$$

2.2.3. Hartree Fock approximation:

In 1930, Vladimir Fock identified a key limitation of the Hartree equations: they do not enforce the required antisymmetry of the total wave function. This issue is resolved by introducing the Slater determinant, which ensures that the many-electron wave function satisfies the antisymmetry condition. In this framework, the total wave function is constructed from one-electron wave functions arranged in a determinant form:

$$\psi(\vec{r}_1, \vec{r}_2, \ldots\ldots, \overrightarrow{r_N}) = \frac{1}{\sqrt{N!}}\begin{vmatrix} \phi_1(\vec{r}_1)\phi_1(\overrightarrow{r_2}) \ldots & \phi_1(\vec{r}_N) \\ \phi_2(\vec{r}_1)\phi_2(\overrightarrow{r_2}) \ldots & \phi_1(\vec{r}_N) \\ . \quad . & . \\ . \quad . & . \\ \phi_N(\vec{r}_1)\phi_N(\overrightarrow{r_2}) \ldots & \phi_1(\vec{r}_N) \end{vmatrix} \quad \text{(II.14)}$$

This is the easiest way to respect the Pauli's exclusion principle. Themono-electronic equations are written:

$$\left[-\frac{\nabla^2}{2} + \hat{V}_{ext}(\vec{r}) + \hat{V}_i(\vec{r})\right]\phi_i(\vec{r}) + \int d\vec{r}' V_X(\vec{r},\vec{r}')\phi_i(\vec{r}') = \varepsilon_i\phi_i(\vec{r}) \quad \text{(II.15)}$$

By simplifying the equation:

$$h_i\phi_i(\vec{r}) + \int d\vec{r}' V_X(\vec{r},\vec{r}')\phi_i(\vec{r}') = \varepsilon_i\phi_i(\vec{r}) \quad \text{(II.16)}$$

With $V_X(\vec{r},\vec{r}') = -\sum_j \frac{\phi_j{}^*(\vec{r}')\phi_j(\vec{r})}{|\vec{r}-\vec{r}'|}$: The Hartree Fock exchange potential

In quantum physics, the exchange (VX) potential arises as a direct consequence of the Pauli Exclusion Principle, which prevents two electrons from occupying the same quantum state. Within the Hartree–Fock method, the electronic structure is described through two coupled contributions: the local Hartree term and the non-local exchange (Fock) term.

The exchange potential is non-local in nature, meaning it depends on the coordinates of another electron, often introduced through an additional variable r′. This non-locality significantly increases the computational complexity of the Hartree–Fock equations, making their numerical solution more demanding.

For this reason, Density functional theory is frequently preferred in practical calculations, as it reformulates the many-body problem in terms of the electron density rather than the full many-electron wave function, greatly simplifying the computational effort while maintaining good accuracy in many systems.

2.3. Density functional theory:

Density functional theory (DFT) is based on the fundamental idea of using the electron density as the central quantity, in contrast to the Hartree–Fock method, which relies on the many-electron wave function. This change in perspective significantly reduces the complexity of calculations.

Indeed, the electronic wave function depends on 3N variables (the spatial coordinates of all N electrons), whereas the electron density depends only on three spatial variables (x, y, z).This simplification makes computations much more efficient. However, it raises an important question: can all the essential physical information be extracted solely from the electron density?

This question was answered by Pierre Hohenberg and Walter Kohn, who established the foundational theorems demonstrating that the ground-state properties of a many-electron system are uniquely determined by its electron density. Since their work, DFT has become

one of the most widely used methods in computational physics and chemistry, leading to major advances in molecular physics and solid-state physics.

2.3.1. Electron density:

In quantum mechanics, it is not possible to localize an electron as a single particle at a precise position [9, 10]. Instead, one can describe the probability of finding an electron within an infinitesimal volume element d3r⃗. This probability is given by the electron density, which is related to the square of the wave function:

$$\Psi(\vec{r}) \Leftrightarrow \Psi^2(\vec{r}) = \rho(\vec{r}) \qquad \text{(II.17)}$$

This definition ensures that ρ(r⃗) is always positive and represents the probability density of finding an electron at position r⃗. The electron density has several important properties:

- ✓ $\int \rho(\vec{r}) d\vec{r} = N$ (Integration over the entire space), while N is total number of electrons
- ✓ $\rho(\mathrm{r} = \infty) = 0$
- ✓ $\rho(\vec{r})$is an observable *that* can be measured experimentally (by X-ray diffraction)

All these properties indicate that the electron density alone is sufficient to determine the fundamental characteristics of an atomic system. This is the central idea underlying Density functional theory.

2.3.2. Hohenberg-Kohn (HK) theorems:

DFT is founded on two fundamental theorems established in 1964 by Pierre Hohenberg and Walter Kohn [11, 12].

a. Theorem I

For a system of interacting electrons in an external potential $V_{ext}(\mathrm{r}⃗)$, the ground-state electron density ρ(r⃗) uniquely determines this potential (up to an additive constant). In other words, the external potential is a unique functional of the electron density.

Proof: Assume that there exist two different external potentials $V_{ext}(\mathrm{r}⃗)$ and $V'_{ext}(\mathrm{r}⃗)$, differing by more than a constant, which produce the same ground-state density $\rho_0(\mathrm{r}⃗)$. These potentials correspond to two different Hamiltonians $\hat{H}$ and $\hat{H}'$, with distinct ground-state wave functions Ψ and Ψ′, satisfying:

$$\hat{H}\Psi = E_0\Psi \,, \qquad \hat{H}'\Psi' = E_0'\Psi'$$

Since Ψ′ is not the ground state of $\hat{H}$, the variational principle implies:

$$E_0<\langle\Psi'|\hat{H}|\Psi'\rangle \quad \text{(I.18)}$$

$$<\langle\Psi'|\widehat{H'}|\Psi'\rangle + \langle\Psi'|\hat{H} - \widehat{H'}|\Psi'\rangle \quad \text{(II.19)}$$

$$<E'_0 + \int \rho_0(r)[\mathrm{V_{ext}}(\vec{r}_i) - V'_{\mathrm{ext}}(\vec{r}_i)]\overrightarrow{dr} \quad \text{(II.20)}$$

Similarly: $$E'_0<\langle\Psi|\widehat{H'}|\Psi\rangle \quad \text{(I.21)}$$

$$<\langle\Psi|\widehat{H'}|\Psi\rangle + \langle\Psi|\widehat{H'} - \hat{H}|\Psi\rangle \quad \text{(II.22)}$$

$$<E_0 + \int \rho_0(r)[V'_{\mathrm{ext}}(\vec{r}_i) - \mathrm{V_{ext}}(\vec{r}_i)]\overrightarrow{dr} \quad \text{(II.23)}$$

Adding Eq. (VI.2.A.3) and (VI.2.A.6) lead to the contradiction

$$E_0 + E'_0<E'_0 + E_0 \quad \text{(II.24)}$$

Therefore, it is impossible for two different external potentials $\mathrm{V_{ext}}(\vec{r}_i)$ to produce the same ground-state density $\rho_0(\vec{r})$, This means that the ground-state density uniquely determines the external potential, up to an additive constant.

Consequently, the fundamental quantity is no longer the many-electron wave function, but rather the electron density itself, which fully characterizes the ground state and all its properties. This result forms the basis for the second theorem of Pierre Hohenberg and Walter Kohn.

b. **Theorem** 2:

A universal energy functional E[ρ] can be defined in terms of the electron density. The exact ground state of the system corresponds to the minimum value of this functional.

Proof: From the first theorem, the external potential is uniquely determined by the electron density. Since this potential, in turn, uniquely determines the ground-state wave function (except in degenerate cases), all physical observables—such as the kinetic and interaction energies—are also uniquely determined by the density.

As a result, the total energy of the system can be expressed as a functional of the electron density:

$$E[\rho(\vec{r})] = [\hat{T}] + [\hat{V}_{int}] + \int V_{ext}(\rho(\vec{r}))\overrightarrow{dr} \quad \text{(II.25)}$$

$$= F[\rho(\vec{r})] + \int V_{ext}(\rho(\vec{r}))\overrightarrow{dr} \quad \text{(II.26)}$$

Where $F[\rho(\vec{r})]$ is a universal functional. In the ground state the energy is defined by the unique ground state density $\rho_0(\vec{r})$

$$E_0 = E[\rho_0(\vec{r})] = \langle \Psi | \hat{H} | \Psi \rangle \quad \text{(II.27)}$$

By the variational principle, a different density$\rho'(\vec{r})$ will necessarily give a higher energy

$$E_0 = \langle \Psi | \hat{H} | \Psi \rangle < \langle \Psi' | \hat{H} | \Psi' \rangle = E' \quad \text{(II.28)}$$

It follows that, by minimizing the total energy functional with respect to the electron density $\rho(\vec{r})$, one obtains the ground-state energy of the system. The density that achieves this minimum is therefore the true ground-state density.

The practical implementation of this variational principle is provided by the equations developed by Walter Kohn and Lu Jeu Sham [13, 14], commonly known as the Kohn–Sham equations, which offer an effective and tractable approach to solving this problem.

2.3.3. Kohn-Sham equation:

The Kohn–Sham equations provide a practical implementation of Density functional theory by translating the Hohenberg–Kohn theorems into a computational framework. This approach was so impactful that Walter Kohn was awarded the Nobel Prize in Chemistry in 1998.

The Kohn–Sham method maps the original interacting electron system, characterized by the external potential V_{ext} , onto an equivalent fictitious system of non-interacting electrons moving in an effective potential V_{eff}. This auxiliary system is constructed such that it reproduces the same ground-state electron density as the real interacting system. Since the exact forms of the kinetic energy T[ρ] and the electron–electron interaction energy $V_{int}[\rho]$ are not explicitly known, Walter Kohn and Lu Jeu Sham proposed to decompose these terms. In particular, the kinetic energy functional is written as:

$$T[\rho(\vec{r})] = T_0[\rho(\vec{r})] + (T[\rho(\vec{r})] - T_0[\rho(\vec{r})]) \quad \text{(II.29)}$$

which can be expressed as:

$$= T_0[\rho(\vec{r})] + E_c[\rho(\vec{r})] \quad \text{(II.30)}$$

Here, $T_0[\rho]$ is the kinetic energy of the non-interacting reference system, while $E_0[\rho]$ represents the correlation energy, accounting for the difference between the true interacting system and the non-interacting approximation.

Where $T_0[\rho(\vec{r})]$: The kinetic energy of non-interacting electron gas. $E_c[\rho(\vec{r})]$: the correlation energy that is neglected in the Hartree-Fock approximation.

$$V_{int}[\rho(\vec{r})] = E_H[\rho(\vec{r})] + (V_{int}[\rho(\vec{r})] - E_H[\rho(\vec{r})]) \quad \text{(I.31)}$$

$$= E_H[\rho(\vec{r})] + E_x[\rho(\vec{r})] \quad \text{(I.32)}$$

Where$E_H[\rho(\vec{r})]$: Term of Hartree.$E_x[\rho(\vec{r})]$: Exchange energy that is neglected by Hartree. Then:

$$F[\rho(\vec{r})]=T_0[\rho(\vec{r})]+E_c[\rho(\vec{r})]+E_H[\rho(\vec{r})]+E_x[\rho(\vec{r})] \quad \text{(II.33)}$$

$$F[\rho(\vec{r})]=T_0[\rho(\vec{r})]+E_H[\rho(\vec{r})]+E_{xc} \quad \text{(II.34)}$$

Therefore, the functional energy of Hohenberg and Kohn can be expressed by the following equation:

$$E[\rho(\vec{r})]=T_0[\rho(\vec{r})]+E_H[\rho(\vec{r})]+E_{xc}[\rho(\vec{r})]+\int \rho(\vec{r})V_{ext}(\vec{r})d\vec{r} \quad \text{(II.35)}$$

With $E_{XC}[\rho(\vec{r})]$: Exchange-correlation energy, is due to the difference between the non-interacting and the interacting kinetic energies as well as to the difference between real interaction energy and that of Hartree. The equations of Kohn and Sham that solve the problem is :

$$\left[-\frac{h^2}{2m_e}\vec{\nabla}_i^2+V_{eff}(\vec{r})\right]\varphi_i(\vec{r})=\varepsilon_i\varphi_i(\vec{r}) \quad \text{,i=1,……N} \quad \text{(II.36)}$$

Where there is one electron in each of the N orbitals $\varphi_i(\vec{r})$, with the lowest eigenvaluesε_i. The density of the auxiliary system is constructed from:

$$\rho(\vec{r})=\sum_{i=1}^{N}|\varphi_i(\vec{r})|^2 \quad \text{(II.37)}$$

The effective potential is of the form:

$$V_{eff}(\vec{r})=V_{ext}[\rho(\vec{r})]+V_H[\rho(\vec{r})]+V_{xc}[\rho(\vec{r})] \quad \text{(II.38)}$$

With

$$V_H[\rho(\vec{r})]=\frac{1}{2}\int\frac{e^2}{4\pi\varepsilon_0}\frac{\rho(\vec{r}')}{|\vec{r}-\vec{r}'|}d^3\vec{r}' : \text{Hartree potential}$$

$$V_{xc}[\rho(\vec{r})]=\frac{\delta E_{xc}[\rho(\vec{r})]}{\delta\rho(\vec{r})} : \text{Exchange}-\text{correlation potential}$$

So far, Density functional theory (DFT) provides, in principle, an exact framework for describing many-electron systems. However, for practical applications, it is necessary to introduce an explicit form for the exchange–correlation functional $E_{xc}[\rho(\vec{r})]$, which is not known exactly. Therefore, approximations to $E_{xc}[\rho(\vec{r})]$ are required, and these approximations are central to making DFT computationally feasible and widely applicable..

2.3.4. Solving Kohn-Sham equations

The Kohn–Sham equations provide a practical way to obtain the ground-state energy and electron density of a many-electron system using an independent-particle approach. However, these equations must be solved self-consistently, since the effective potential $V_{eff}(\vec{r})$ depends on the electron density $\rho(\vec{r})$ are closely related. This is usually done numerically through some self-consistent iteration as shown in Figure (01)
Discovering an appropriate resolution can be achieved by adhering to these procedures:

- Start with an initial guess for the electron density $\rho(\vec{r})$.
- Compute the effective potential $V_{eff}(\vec{r})$.
- Solve the Kohn–Sham equations to obtain single-particle eigenvalues and wave functions.
- Construct a new electron density from the obtained wave functions.
- Check the self-consistency condition by comparing the new density with the previous one.
- If convergence is reached, compute physical quantities such as total energy and forces; otherwise, repeat the cycle.

2.4. Methodology

In this section, we present the fundamental concepts of the linearized augmented plane wave method with local orbitals (LAPW+lo), including its different developments related to linearization, full-potential treatment, and the inclusion of local orbitals. We also discuss the treatment of the exchange–correlation potential using common approximations such as LDA, GGA, and GGA+mBJ.

2.4.1. Augmented Plane Wave methods:

Several computational approaches have been developed to determine the electronic, optical, thermal, and mechanical properties of materials. These methods can be classified into three main categories:

- Empirical methods: based on experimental data and fitted parameters derived from observations.
- Semi-empirical methods: combine experimental data with theoretical models to predict properties efficiently, even for large systems.

- **Ab initio methods**: rely solely on fundamental physical principles, without requiring empirical input.

In recent years, *ab initio* methods—also known as "first-principles methods"—have become widely used. Among them, the Full-potential linearized augmented plane wave method (FP-LAPW), developed by Olle Andersen [15], is one of the most accurate techniques. It is an improved version of the earlier augmented plane wave method (APW), offering enhanced precision in electronic structure calculations.

2.4.1.1. APW method:

The Augmented Plane Wave (APW) method is one of the most widely used approaches for solving the electronic structure problem within the framework of the Kohn–Sham (KS) equations. It was first introduced by Slater in 1937 [9, 16]. The central idea of this method is based on the observation that the behavior of electrons depends strongly on their distance from the atomic nuclei. In regions far from the nuclei, the potential varies slowly and electrons behave almost as free particles, making plane waves an appropriate basis. In contrast, in the vicinity of atomic nuclei, the potential becomes strongly varying and electrons exhibit atomic-like behavior, which is better described using localized atomic-type functions.

To account for this dual character, space is divided into two distinct regions: non-overlapping spherical regions centered on each atom with radius R_α , known as muffin-tin spheres S_α, and the remaining volume between these spheres, referred to as the interstitial region III [9].

Within this framework, the APW basis function is defined as:

$$\phi(\vec{r}) = \begin{cases} \varphi_i(\vec{r}) = \frac{1}{\Omega^{\frac{1}{2}}} \sum_G C_G \, e^{i(\vec{k}+\vec{G})\vec{r}} r > R_\alpha \\ \varphi_s(\vec{r}) = \sum_{lm} A_{lm} U_l^\alpha(r, E_l) Y_{lm}(\vec{r}) \, r < R_\alpha \end{cases} \quad \text{(II.39)}$$

From (II.1) φ is the wave function, Ω is the unit cell volume, C_G and $A_{lm}$are expansion coefficients ,$Y_{l,m}$are spherical harmonics ;$U_l^\alpha$is the numerical solution to the radialSchrödinger equation which is given by:

$$\left\{-\frac{d^2}{dr^2} + \frac{l(l+1)}{r^2} + V(r) - E_{nl}\right\} r U_l(r) = 0 \quad \text{(II.40)}$$

Slater's approach relies on the fact that plane waves are suitable solutions of the Schrödinger equation in regions of nearly constant potential, whereas radial functions provide accurate solutions in the spherically symmetric potential near atomic cores. To ensure physical

consistency, the basis functions must be continuous at the muffin-tin boundaries. In the APW formalism, this continuity condition is enforced by determining the radial functions U_l^α through the coefficients C_G obtained from the plane-wave expansion inside the spherical regions.

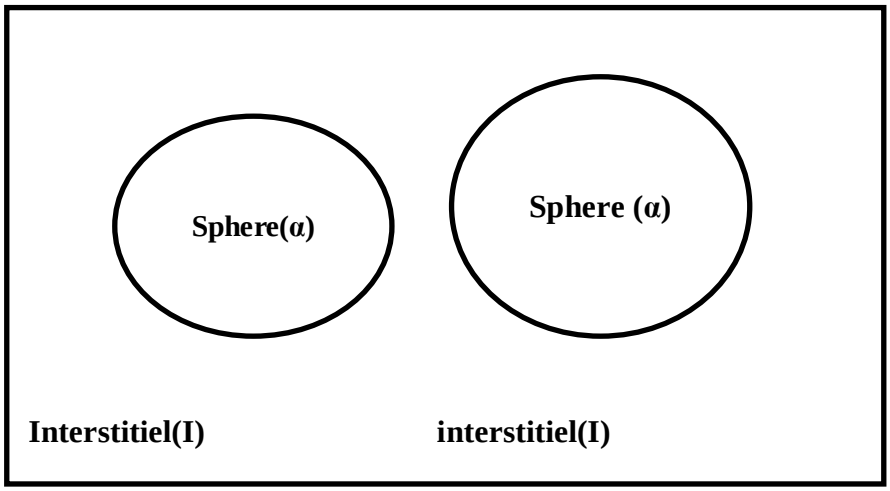

Figure 2-1: *Adaptation of the basis set by dividing the unit cell into atomic spheres and interstitial regions.*

Within the APW formalism, basis functions are constructed to be continuous across the entire crystal volume, including both the interstitial region and the muffin-tin spheres. Although this method is widely used for calculating structural, electronic, optical, and magnetic properties of solids, it presents several inherent limitations.

One major restriction is its reliance on the spherical muffin-tin approximation, which assumes a spherically symmetric potential within atomic spheres and a constant potential in the interstitial region. This approximation can limit the method's accuracy for systems where the potential deviates significantly from spherical symmetry.

Another important drawback arises from the behavior of the basis functions at the muffin-tin boundary. In the original APW formulation, the wave functions themselves remain continuous, but their derivatives are generally discontinuous at the sphere boundaries, leading to a "kink" in the basis representation.

Furthermore, the radial function $U_l^\alpha(r, E_l)$ depends explicitly on the energy, which introduces a nonlinear eigenvalue problem. This energy dependence complicates the numerical solution of the Kohn–Sham equations and may lead to convergence difficulties, particularly in cases where U_l^α becomes very small near the boundary of empty spheres.

To overcome these limitations, several improvements and reformulations of the original APW method have been proposed, most notably by Koe0lling [17]and Andersen [15, 18], leading to more stable and efficient variants of the method.

2.4.1.2. LAPW:

To overcome the difficulties associated with the original APW method—particularly the discontinuity of the derivative of the basis functions at the muffin-tin boundary separating the interstitial and atomic (co0re) regions—linearized methods were developed in the mid-1970s. These approaches were pioneered by Andersen and Koelling together with Arbman [15, 17], building on an idea originally proposed by Marcus. The key improvement introduced by Andersen consists in linearizing the energy dependence of the radial functions within the muffin-tin spheres.

In the Linearized Augmented Plane Wave (LAPW) method, the basis functions inside the muffin-tin (MT) spheres are constructed as linear combinations of the radial solution $U_l(r, E_l)$ and its energy d0erivative $\dot{U}_l(r, E_l)$.The basis functions are defined as:

$$\phi(\vec{r}) = \begin{cases} \varphi_i(\vec{r}) = \frac{1}{\Omega^{\frac{1}{2}}} \sum_G C_G \, e^{i(\vec{k}+\vec{G})\vec{r}} r > R \\ \varphi_s(\vec{r}) = \sum_{lm} \left[A_{lm} U_l(r, E_0) + B_{lm} \dot{U}_l(r, E_0)\right] Y_{lm}(\vec{r}) \, r < R \end{cases} \quad \text{(II.41)}$$

where the B_{lm} coefficients for the energy derivative analogous to theA_{lm}.The basis functions inside the spheres are linear combinations of a radial functions $U_l(r)Y_{lm}(\vec{r})$and their energy derivatives $\dot{U}_l(r)Y_{lm}(\vec{r})$ are the augmenting functions. The U_l are defined as in the APW method **equation (II.1)** and the energy derivative, $\dot{U}_l(r)Y_{lm}(\vec{r})$, satisfies the following equation:

$$\left\{-\frac{d^2}{dr^2} + \frac{l(l+1)}{r^2} + V(r) - E_l\right\} r\dot{U}_l(r) = 0 \quad \text{(II.42)}$$

In contrast to the APW method, where only plane waves are used in the interstitial region, the LAPW method retains plane waves in the interstitial region but employs a more flexible basis inside the muffin-tin spheres through the inclusion of both radial functions and their energy derivatives.

This construction can be interpreted as a first-order Taylor expansion of the radial function around a chosen linearization energy E_l:

$$U_l(r, E) = U_l(r, E_l) + (E - E_0)\dot{U}_l(r - E_0) + O((E - E_l)^2) \quad \text{(II.43)}$$

$$\text{While} \dot{U}_l(r, E_0) = \frac{\partial U_l(r)}{\partial E} \quad \text{(II.44)}$$

As a result of this linearization, the basis set becomes energy-independent, which removes the nonlinear eigenvalue problem present in the APW method. The remaining approximation introduces an error that is quadratic in $(E-E_l)$, leading to eigenvalue errors of fourth order.

Consequently, the LAPW method provides improved numerical stability and ensures both the continuity of the wave function and its derivative at the muffin-tin boundary.

2.4.1.3. APW+LO method:

The APW basis can be further improved by introducing local orbitals, leading to the so-called APW+lo method proposed by Sjöstedt et al [19]. This approach enhances the original APW formalism by increasing the flexibility of the basis set through the addition of local orbitals (lo), while maintaining a computational efficiency comparable to APW. In contrast to LAPW [20], where energy derivatives are included for all angular momentum channels, the APW+lo method introduces these additional functions only for selected quantum numbers.

In this scheme, the basis functions are defined differently inside and outside the muffin-tin (MT) spheres:

$$\phi(\vec{r}) = \begin{cases} 0 & r > R_\alpha \\ \left[A_{lm}U_l(r,E_l) + B_{lm}\dot{U}_l(r,E_l)\right]Y_{lm}(\vec{r}) & r < R_\alpha \end{cases} \quad \text{(II.45)}$$

In this formulation, the coefficients $A_{lm}$and B_{lm} are determined by enforcing the matching conditions at the muffin-tin boundary. Unlike LAPW, the energy derivative function $\dot{U}_l$ is not included for all plane-wave expansions but is introduced selectively as local orbitals for specific angular momentum channels where additional variational flexibility is required.

This selective use of local orbitals improves the efficiency of the basis set. In particular, APW+lo often achieves faster convergence than LAPW while maintaining comparable accuracy for many systems. However, as with LAPW, the method still relies on an energy linearization around a chosen reference energy, and questions regarding the accuracy of this linearization remain relevant, particularly in cases involving strongly varying electronic states [17].

2.4.2. Exchange-potential correlation:

2.4.2.1. Local density approximation (LDA) :

The Local Density Approximation (LDA), introduced by Walter Kohn and Lu Jeu Sham in 1965 [13], is one of the most widely used approximations in density functional theory (DFT). This approach is based on the assumption that the electron density at each point in space can be treated locally as that of a homogeneous (uniform) electron gas.

Within this approximation, the exchange–correlation energy at a given point depends only on the value of the electron density at that point, and is assumed to be equal to the exchange–

correlation energy density of a uniform electron gas with the same density. This leads to the following expression for the exchange–correlation energy functional:

$$E_{xc}^{LDA}[\rho(\vec{r})] = \int \rho(\vec{r})\, \varepsilon_{xc}^{hom}[\rho(\vec{r})] d^3\vec{r} \quad \text{(II.46)}$$

Where$\varepsilon_{xc}^{hom}[\rho(\vec{r})]$: The exchange-correlation energy per particle. The exchange-correlation potential is then given by:

$$V_{xc}[\rho(\vec{r})] = \frac{\delta E_{xc}[\rho(\vec{r})]}{\delta\rho(\vec{r})} = \varepsilon_{xc}^{hom}[(\vec{r})] + \rho(\vec{r})\frac{\delta\varepsilon_{xc}^{hom}[\rho(\vec{r})]}{\delta\rho(\vec{r})} \quad \text{(II.47)}$$

For practical use of the LDA in calculations it is necessary to determine the exchange-correlation energy for a uniform electron gas of a given density. It is common to split $\varepsilon_{xc}(\rho(\vec{r}))$ into exchange and correlation potentials

$$\varepsilon_{xc}(\rho(\vec{r})) = \varepsilon_x(\rho(\vec{r})) + \varepsilon_c(\rho(\vec{r})) \quad \text{(II.48)}$$

The exchange term, commonly referred to Dirac's exchange[21] (symbolized by S, means that this expression was taken over by Slater)

$$\varepsilon_x^S(\rho(\vec{r})) = -\frac{3}{4}\left(\frac{3\rho(\vec{r})}{\pi}\right)^{1/3} \quad \text{(II.49)}$$

The exactly Accurate values for $\varepsilon_x^S(\rho(\vec{r}))$ have been determined from Quantum Monte Carlo (QMC) calculations These have then been interpolated to provide an analytic form for $\varepsilon_c(\rho(\vec{r}))$.

2.4.2.2. Generalized gradient approximations (GGA):

As previously discussed, the Local Density Approximation (LDA) neglects the inhomogeneity of the real electron density. This limitation motivated the development of the Generalized Gradient Approximation (GGA), which incorporates not only the local value of the electron density but also its spatial variation through the density gradient.

In GGA, the exchange–correlation energy is expressed as a functional depending on both the electron density $\rho(\vec{r})$ and its gradient $|\vec{\nabla}\rho(\vec{r})|$:

$$E_{xc}^{GGA}(\rho(\vec{r})) = \int f_{xc}[\rho(\vec{r}), \nabla\rho(\vec{r})] d^3\vec{r} \quad \text{(II.50)}$$

The specific form of the function f_{xc} distinguishes the different GGA functionals. Among the most widely used are those proposed by Axel Becke[22], John Perdew and collaborators [23], as well as the well-known Perdew–Burke–Ernzerhof functional (PBE) [24].

In general, GGA provides improved predictions over LDA for many physical properties, such as bond lengths, binding energies, and lattice constants, particularly in

systems where the electron density varies rapidly. However, GGA may sometimes overcorrect LDA results. For example, in certain ionic crystals, LDA yields lattice parameters in good agreement with experimental data, whereas GGA tends to slightly overestimate them.

Despite these improvements, both LDA and GGA remain insufficient for describing systems with strong electron localization and correlation, such as transition metal oxides and rare-earth compounds. This limitation has led to the development of more advanced approaches beyond standard LDA and GGA.

2.4.2.3. GGA+mBJ:

To improve the accuracy of band gap predictions within density functional theory, Fabien Tran and Peter Blaha [25, 26] proposed a modified version of the Becke–Johnson exchange potential [16], known as the modified Becke–Johnson (mBJ) potential **.** The mBJ approximation enhances the description of the exchange potential, leading to a significant improvement in the calculated band gaps. Unlike LDA and GGA, which typically underestimate band gaps, the mBJ approach generally produces values that are much closer to experimental results [9].

This method has proven effective across a wide range of materials, including semiconductors with small band gaps and insulators with large gaps. As a result, the GGA+mBJ scheme has become a popular and efficient alternative for band structure calculations when accurate gap estimation is required.

References

1. Thomas, L.H. *The calculation of atomic fields*. in *Mathematical proceedings of the Cambridge philosophical society*. 1927. Cambridge University Press.
2. Fermi, E., *Statistical method to determine some properties of atoms.* Rend. Accad. Naz. Lincei, 1927. **6**(602-607): p. 5.
3. Hartree, D.R. *The wave mechanics of an atom with a non-Coulomb central field. Part I. Theory and methods*. in *Mathematical Proceedings of the Cambridge Philosophical Society*. 1928. Cambridge university press.
4. Dirac, P.A.M., *Quantum mechanics of many-electron systems.* Proceedings of the Royal Society of London. Series A, Containing Papers of a Mathematical and Physical Character, 1929. **123**(792): p. 714–733.
5. Fock, V. and D. Iwanenko, *Quantun linear geometry and parallel transfer.* CR Acad, 1929. **188**: p. 1470.
6. Schrödinger, E., *An undulatory theory of the mechanics of atoms and molecules.* Physical review, 1926. **28**(6): p. 1049.
7. Tully, J.C., *Perspective on "Zur Quantentheorie der Molekeln" Born M, Oppenheimer R (1927) Ann Phys 84: 457.* Theoretical chemistry accounts, 2000. **103**(3): p. 173–176.
8. **GIUSTINO**, F., *Materials modelling using density functional theory: properties and predictions*. 2014: Oxford University Press.
9. Slater, J.C., *Wave functions in a periodic potential.* Physical Review, 1937. **51**(10): p. 846.
10. Heisenberg, W., *The actual content of quantum theoretical kinematics and mechanics*. 1983.
11. Hohenberg, P. and W. Kohn, *Inhomogeneous electron gas.* Physical review, 1964. **136**(3B): p. B864.
12. Hedin, L. and S. Lundqvist, *Effects of electron-electron and electron-phonon interactions on the one-electron states of solids*, in *Solid state physics*. 1970, Elsevier. p. 1–181.
13. Kohn, W. and L.J. Sham, *Self-consistent equations including exchange and correlation effects.* Physical review, 1965. **140**(4A): p. A1133.
14. Cuevas-Saavedra, R. and V.N. Staroverov, *Exact expressions for the Kohn–Sham exchange-correlation potential in terms of wave-function-based quantities.* Molecular Physics, 2016. **114**(7-8): p. 1050–1058.
15. Andersen, O.K., *Linear methods in band theory.* Physical Review B, 1975. **12**(8): p. 3060.
16. Slater, J., *Energy band calculations by the augmented plane wave method*, in *Advances in quantum chemistry*. 1964, Elsevier. p. 35–58.
17. Koelling, D. and G. Arbman, *Use of energy derivative of the radial solution in an augmented plane wave method: application to copper.* Journal of Physics F: Metal Physics, 1975. **5**(11): p. 2041–2054.
18. Anisimov, V.I., J. Zaanen, and O.K. Andersen, *Band theory and Mott insulators: Hubbard U instead of Stoner I.* Physical Review B, 1991. **44**(3): p. 943.
19. Sjöstedt, E., L. Nordström, and D. Singh, *An alternative way of linearizing the augmented plane-wave method.* Solid state communications, 2000. **114**(1): p. 15–20.
20. Madsen, G.K., et al., *Efficient linearization of the augmented plane-wave method.* Physical Review B, 2001. **64**(19): p. 195134.

21. Dirac, P.A. *Note on exchange phenomena in the Thomas atom*. in *Mathematical proceedings of the Cambridge philosophical society*. 1930. Cambridge University Press.
22. Becke, A.D., *Density-functional exchange-energy approximation with correct asymptotic behavior.* Physical review A, 1988. **38**(6): p. 3098.
23. Perdew, J.P., et al., *Atoms, molecules, solids, and surfaces: Applications of the generalized gradient approximation for exchange and correlation.* Physical review B, 1992. **46**(11): p. 6671.
24. Perdew, J.P., K. Burke, and M. Ernzerhof, *Generalized gradient approximation made simple.* Physical review letters, 1996. **77**(18): p. 3865.
25. Becke, A.D. and E.R. Johnson, *A simple effective potential for exchange.* The Journal of chemical physics, 2006. **124**(22).
26. Tran, F., P. Blaha, and K. Schwarz, *Band gap calculations with Becke–Johnson exchange potential.* Journal of Physics: Condensed Matter, 2007. **19**(19): p. 196208.

CHAPTER III

METHODS OF SYNTHESIS

3.1. Introduction

The rise of soft chemistry emerged during the 1974 energy crisis. At that time, the scientific community sought to employ synthesis methods that consume less energy to create materials. This approach benefited from advances in analytical instrumentation. Thanks to these developments, scientists were able to examine materials in detail, for example using electron microscopes.[1]

Solid-state chemistry offers numerous methods for producing materials such as mixed oxides. spinels, perovskites, and pyrochlores are examples of such materials. The properties of these materials, including their structure and morphology, depend on the preparation method. Synthesis conditions and the temperature employed also play an important role[1].

3.2. Co-precipitation

Co-precipitation is a soft-chemistry method that differs from other approaches such as precursor decomposition, microemulsions, or the sol–gel process. It enables the production of large quantities of powders and the attainment of grain sizes on the nanometer scale.

To obtain powders with controlled particle size distribution, precise stoichiometry, and high purity, two main steps must be followed. The first step is the precipitation itself, which constitutes the fundamental stage of soft chemistry. It allows either the direct formation of the desired mixed oxide or the generation of precursors composed of oxides or hydroxides of the involved metals. The second step consists of one or more thermal treatments, which are necessary to remove adsorbed residues on the particle surface and to achieve the formation of the final desired compound[2].

The control of morphology, particle size, and size distribution of particles obtained by co-precipitation depends on the mastery of the different kinetic stages of the process. These stages include the formation of a precursor capable of condensation, nucleation, the growth of nuclei through condensation, and particle aging.

The control of these steps is ensured by regulating key experimental parameters such as pH, reactant concentration, and temperature[3].

3.3. Solid-State Reaction Synthesis

Solid-state reaction is the most classical preparation method and is still widely used in industry. It consists of mixing several solid oxides and heating them at temperatures below their melting points, so that the chemical reaction proceeds entirely in the solid state[4].

This reaction begins at the interfaces between solid grains and progresses through the diffusion of reactive species from the core of the particles toward the interfacial regions. An increase in temperature enhances this diffusion phenomenon, which is generally the rate-limiting step of the process[5, 6].

Despite its simplicity and widespread use, this method presents several drawbacks. Among these is a relatively slow reaction kinetics, which strongly depends on thermal conditions such as the heating rate and annealing time. Another limitation is the requirement for high temperatures, leading to significant energy consumption. Finally, chemical homogeneity may sometimes be insufficient, resulting in a final product whose composition deviates from the targeted stoichiometry[6].

3.4. Sol–gel method

The term “sol–gel” originates from the combination of the words “solution” and “gelation.” Before transforming into a gel, the mixture is liquid and consists of colloidal oligomers, small macromolecules, and partially hydrolyzed monomers, depending on the degree of polymerization. This stable dispersion of colloidal particles in a liquid is called a “sol.” The particle size must be sufficiently small for dispersive forces to overcome gravity, even when the particles are denser than the surrounding medium [7].

A gel is a three-dimensional oxide network filled with solvent. Its mechanical cohesion is ensured by chemical bonds that impart a certain rigidity to the material. This network forms through interactions of the Van der Waals type. The transition from the “sol” state to the “gel” state occurs over a period known as the gelation time. However, the reactions responsible for gelation continue even beyond this point[8].

Two main approaches can be identified for synthesizing materials via the sol–gel method:

- The first approach is referred to as the inorganic or colloidal method. It uses metal salts such as chlorides or nitrates in an aqueous solution. Although this approach is inexpensive, it is difficult to control, which limits its applications.

- The second approach is known as the metallo-organic or polymeric method. It employs metal alkoxides in an organic medium. This method is more costly, but it provides better control over particle size.

In both cases, the process begins with a hydrolysis reaction that forms M–OH groups, followed by condensation reactions that produce M–O–M bonds.

Materials obtained by this method exhibit high purity, excellent homogeneity, high density, and a large specific surface area. The grain size can be extremely fine, below 10 nm, and the temperatures required for synthesis are relatively low[9]

References

1. Yoshimura, M. and J. Livage, *Soft processing for advanced inorganic materials.* MRS Bulletin, 2000. **25**(9): p. 12–13.
2. Mondal, D., *Covalently Crosslinked Organic/Inorganic Hybrid Biomaterials for Bone Tissue Engineering Applications*. 2018, The University of Western Ontario (Canada).
3. Mullin, J.W., *Crystallization*. 2001: Elsevier.
4. West, A.R., *Solid state chemistry and its applications*. 2022: John Wiley & Sons.
5. Shewmon, P., *Atomic theory of diffusion*, in *Diffusion in solids*. 2016, Springer. p. 53–96.
6. Callister Jr, W.D. and D.G. Rethwisch, *Materials science and engineering: an introduction*. 2020: John wiley & sons.
7. Brinker, C.J. and G.W. Scherer, *Sol-gel science: the physics and chemistry of sol-gel processing*. 1990: Gulf Professional Publishing.
8. Levy, D. and M. Zayat, *The Sol-Gel Handbook, 3 Volume Set: Synthesis, Characterization, and Applications*. Vol. 2. 2015: John Wiley & Sons.
9. Wright, J.D. and N.A. Sommerdijk, *Sol-gel materials: chemistry and applications*. 2018: CRC press.

CHAPTER IV
RESULTS AND DISCUSSIONS

4.1. Introduction

Spinel oxides with the general formula AB_2O_4 represent a highly versatile and extensively studied class of crystalline materials, distinguished by their robust cubic or tetragonal lattice structures, which give rise a wide spectrum of functional properties, including magnetic, electronic, optical, and catalytic behaviors [1-6]. Their broad applicability across domains such as catalysis, magnetism, energy storage, and electronic devices stems largely from the intrinsic crystallographic flexibility of the spinel framework[7-9].

This versatility arises from the structure's ability to host a diverse range of cationic species within specific crystallographic sites namely, the tetrahedral (A) and octahedral (B) positions. Such flexibility allows for precise control over the electronic configuration, magnetic coupling, and ionic transport properties, enabling systematic tuning of material behavior to meet application-specific requirements[10].

Structurally, most spinel compounds crystallize in the cubic Fd-3m space group, adopting the so-called normal spinel configuration, wherein A-site cations occupy tetrahedral sites, and B-site cations are coordinated octahedrally within the oxygen sublattice [11]. This ordered yet flexible cationic arrangement forms a stable structural backbone that supports extensive cation substitution, making spinels a powerful platform for rational materials design [12-14].

Among these compounds, $CuMn_2O_4$ has attracted significant attention due to its multifunctional characteristics, including structural complexity, electrical conductivity, catalytic activity, and magnetic ordering. Fang et al. [15] demonstrated its effectiveness in NH_3–SCR catalysis, citing high Mn^{3+} content and synergistic Cu–Mn interactions as key contributors to NO_x conversion. Patra et al. [16] found that Ti-doped $CuMn_2O_4$ transitions from ferrimagnetic (~76 K) to spin-glass behavior. Al-Hadded et al. [17] observed cluster-glass dynamics at ~40 K and a ferromagnetic transition at ~80 K in $Cu_{1.5}Mn_{1.5}O_4$, accompanied by a magnetic entropy change suitable for magnetic refrigeration. Recently, $CuMn_2O_4$ has also been reported as an efficient catalyst for the aerobic oxidation of 5-hydroxymethylfurfural to FDCA with a 92% yield, attributed to Mn-rich surfaces and dual-valence states (Cu^{2+}/Cu^{+}, Mn^{4+}/Mn^{3+}) [18].

In this work, we conduct a combined theoretical and experimental study of $CuMn_2O_4$ normal spinel. First-principles calculations based on the Full-Potential Linearized Augmented Plane Wave (FP-LAPW) [19]method within the density functional theory (DFT) framework are used to investigate structural stability, electronic structure, and magnetic behaviour. Additionally, experimental synthesis and X-ray diffraction (XRD) measurements are carried out to validate the theoretical models and gain deeper insight into the structural properties of this spinel-type material.

4.2. Experimental methods:

4.2.1. Synthesis of $CuMn_2O_4$

$CuMn_2O_4$ spinel oxide was synthesized using sol-gel-based method: For the preparation of $CuMn_2O_4$, a conventional sol-gel route was employed [20, 21]. Stoichiometric amounts of copper nitrate trihydrate ($Cu(NO_3)_2 \cdot 3H_2O$, 99+%, Sigma Aldrich, USA) and manganese nitrate tetrahydrate $Mn(NO_3)_2 \cdot 4H_2O$, 98+%, Sigma Aldrich, USA) were dissolved in 50 mL of distilled water under continuous stirring. Citric acid was then added as a chelating agent, with a molar ratio of 1:2 relative to the total metal cations. The resulting solution was heated at 85 °C until a viscous gel get formed, followed by drying at 120 °C for 12 h to obtain a xerogel. The precursor was decomposed at 350 °C in air for 3 h and allowed to cool to room temperature. The obtained intermediate was finely ground in an agate mortar and subsequently calcined at 800 °C for 2 h. Finally, the product was reground to obtain homogeneous $CuMn_2O_4$ powder.

4.2.2. Characterization Technique

The crystal structure and phase purity of the synthesized powders were investigated by X-ray diffraction (XRD) using a Rigaku D-Max/B diffractometer equipped with **a Cu-Kα** radiation source (**λ** = 0.15406$ nm). The diffraction patterns were recorded over a 2θ range of 20°–80° with a step size of 0.02°. The obtained data was used to confirm the formation of the spinel phase and to calculate the lattice parameters.

4.3. Computational Details

First-principles calculations were carried out using the full-potential linearized augmented plane wave (FP-LAPW) method[22] within the density functional theory (DFT) framework[23, 24], as implemented in the WIEN2k code[25]. The generalized gradient approximation (GGA)[26] was employed for structural optimization, while both GGA and GGA combined with the modified Becke–Johnson potential (GGA+mBJ)[27] were used to investigate the electronic and magnetic properties. For all studied compounds, the plane-wave cutoff parameter was set to $R_{Kmax} = 8$, with an angular momentum cutoff of $l_{max} = 10$ inside the muffin-tin spheres, and a Fourier expansion cutoff of $G_{max} = 12$ a.u^{-1}. The energy separation between core and valence states was set to 7 Ry. The muffin-tin radii were chosen as 1.95 a.u. for Cu, 1.89 a.u. for Mn and 1.63 a.u. for O atoms. The convergence criteria for self-consistency were set to 10^{-5} Ry for total energy, 10^{-4} e for charge, and 0.1 mRy/a.u. for atomic forces.

4.4. Results and Discussions

4.4.1. Experimental results: X-ray Diffraction

The obtained XRD patterns, which confirm the formation of the $CuMn_2O_4$, and $CoCuMnO_4$ spinel phases, are shown in **Figures 1** and 2.

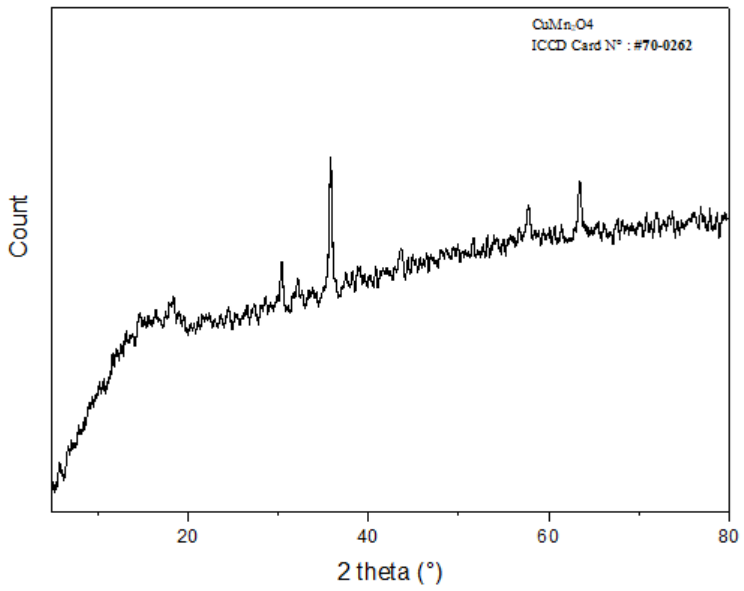

Figure 4 1: *XRD pattern of $CuMn_2O_4$. Single-phase cubic spinel (Fd-3m, a = 8.28 Å). (311) reflection used as structural constraint for FP-LAPW calculations*

The structural characterization of $CuMn_2O_4$ using X-ray diffraction (XRD) confirms the successful formation of a single-phase cubic spinel structure belonging to the *Fd3m* space group. All observed diffraction peaks are well indexed to this structure, indicating high crystallinity and phase purity. A key structural parameter, the lattice constant (*a*), was determined using the most intense diffraction peaks, particularly the (311) and (440) planes. The calculated value is: a = 8.28 Å , this value is in excellent agreement with reported literature values (8.28–8.33 Å), confirming that the synthesized material is stoichiometric and structurally consistent with standard copper manganite spinels.

Importantly, the XRD pattern shows no secondary phases, as evidenced by the absence of impurity peaks such as: Mn_2O_3 (~33°) ,CuO (~38.7°) this confirms that the synthesis method successfully produced a pure $CuMn_2O_4$ phase without oxide segregation.

Further structural insight is obtained from the oxygen positional parameter (u = 0.260). This value slightly deviates from the ideal spinel value (~0.25), indicating a distortion in the lattice. This distortion is attributed to the Jahn–Teller effect **of Cu^{2+} ions**, which induces local structural deformation due to electronic instability in the d-orbitals. As a result, oxygen ions shift from their ideal positions, leading to a non-perfect cubic symmetry at the local scale. On the microstructural level, the average crystallite size was estimated using Scherrer's equation applied to the (311) peak. The result shows: Crystallite size ≈ 32.3 nm, this nanoscale size suggests a relatively fine microstructure, which can significantly influence physical properties such as magnetic behavior and electrical conductivity

***Table 4- 1**: Comparative Structural and Microstructural Parameters of the Synthesized Spinel.*

Sample	Reflection (hkl)	Position 2θ (∘)	d-spacing (Å)	FWHM (∘)	Lattice Parameter *a* (Å)
$CuMn_2O_4$	(311)	35.79	2.507	0.27	8.28

4.4.2. Theoretical Results

4.4.2.1. Calculated Structural Parameters: Theoretical lattice parameters and atomic positions

To comprehend the theoretical investigation of the structural properties of $CuMn_2O_4$, calculations were performed using first-principles methods within the Generalized Gradient Approximation (GGA) framework [22], as implemented in the Wien2k code [23]. The calculated lattice parameters demonstrate excellent agreement with our experimental data obtained via XRD, thereby validating the computational approach employed.

Analysis of the oxygen positional parameter ('u') reveals subtle yet significant distortions from the ideal spinel structure. Furthermore, variations in the bulk modulus (B) provide insight into the mechanical response and incompressibility of the material. The analysis of total energy contributes to understanding the thermodynamic stability of the compound. These findings offer critical atomic-level insights into the fundamental structural characteristics of this technologically relevant spinel material.

Structurally, spinels are based on a cubic close-packed (c.c.p.) array of oxygen anions, with A and B cations occupying specific interstitial sites. Specifically, A cations typically occupy one-eighth of the tetrahedrally (T) coordinated sites, while B cations occupy one-half of the octahedrally (M) coordinated sites. Understanding the precise structural parameters, including lattice constants and atomic positions, is fundamental, as these parameters determine interatomic distances and bond angles, which in turn govern the electronic structure, bonding characteristics, and ultimately the macroscopic physical properties of the material under various conditions [24].

This investigation focuses on the structural properties of $CuMn_2O_4$. Figure 3 illustrates the crystal structure of the studied spinel compound. The compound is known to adopt a normal spinel structure. A detailed analysis of its structural parameters is essential to elucidate its intrinsic properties and to provide a solid foundation for further theoretical and experimental studies.

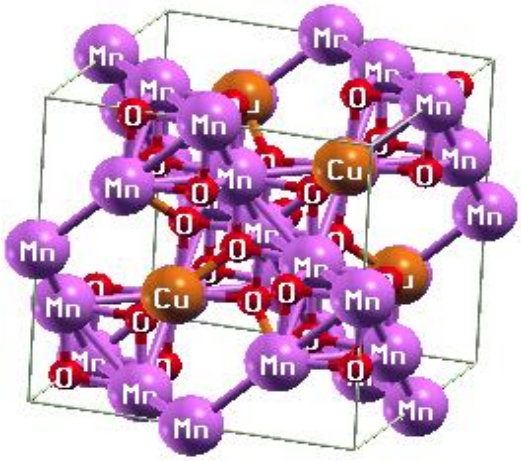

***Figure 4-2**: Crystal structures of CuMn2O4 Spinel Compounds*

To determine the equilibrium structural parameters, comprehensive structural optimizations were carried out for **$CuMn_2O_4$**. This involved minimizing the total energy of the system with respect to both the unit cell volume and the internal atomic positions.

The resulting energy–volume curve (as shown in Figure 4), which exhibits a clear minimum, was then fitted to the Birch–Murnaghan equation of state [22, 23] to accurately determine

the equilibrium lattice parameter, bulk modulus, and its pressure derivative, thereby confirming the structural stability at the equilibrium volume.

Typical convergence criteria for energy, forces, and charge density were rigorously applied to ensure the accuracy and reliability of the calculated results.

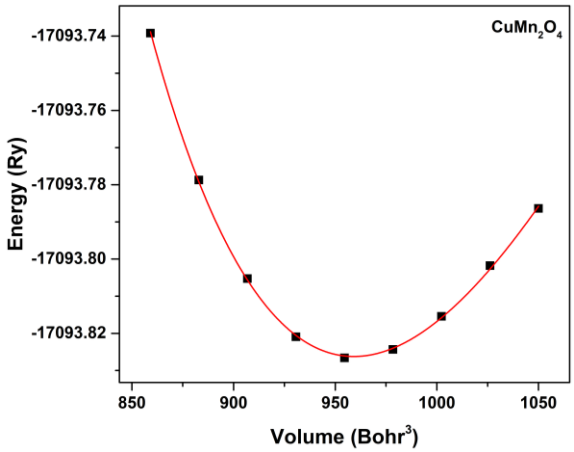

Figure 4 3: *Energy–Volume Curves of $CuMn_2O_4$ Normal Spinel*

The structural properties derived from the Generalized Gradient Approximation (GGA) calculations using the Wien2k code, alongside our experimental data obtained via XRD, are summarized in **Table 2.** This table provides a consolidated view of the lattice parameter (*a*), oxygen positional parameter (*u*), bulk modulus (*B*), and its pressure derivative (*B'*) for the studied spinel compound.

Table 4- 2: *Calculated (GGA) and Experimental Structural Parameters of CuMn2O4 Spinel Compound*

Compounds	*a(Bohr)*	*U*	*B*	*B'*
$CuMn_2O_4$	GGA : 15.66 Exp : 15.69 15,769[28]	0.265 0.261	179.9732	7.6033

The calculated lattice parameter provides a fundamental measure of the unit cell dimensions for $CuMn_2O_4$, the GGA lattice parameter of 15.66 Bohr shows very good agreement with the experimental value of 15.69 Bohr obtained via XRD. This agreement confirms the reliability of the computational approach. It is well known that GGA calculations may slightly overestimate lattice parameters; however, the small deviation observed here indicates that the chosen computational setup provides an accurate description of the structural properties of this spinel system.

The oxygen positional parameter, denoted as '*u*', is a key structural descriptor in spinel compounds. In the ideal spinel structure, '*u*' equals 0.25. Any deviation from this value

reflects structural distortion from the ideal cubic close-packed arrangement. The calculated value of *u* for $CuMn_2O_4$ is 0.265, which is slightly higher than the experimental value (0.261) and greater than the ideal value. This indicates a noticeable distortion of the oxygen sublattice, leading to modifications in bond lengths and angles within the structure. Such deviations are generally associated with distortions in the octahedral coordination environment and shifts in oxygen positions.

The bulk modulus (*B*) is is an essential mechanical parameter that characterizes the resistance of a material to uniform compression. For $CuMn_2O_4$, the calculated bulk modulus is 179.97 GPa, indicating a relatively good resistance to compression. The pressure derivative of the bulk modulus ($B' = 7.60$) suggests that the material becomes stiffer under increasing pressure.

The relationship between the oxygen positional parameter (*u*) and the mechanical properties provides additional insight into the structure–property interplay. Although an increase in *u* generally reflects structural distortion, its influence on the bulk modulus is not strictly linear. This indicates that, beyond structural distortion, other factors such as cation–oxygen bond strength, ionic radii, and local coordination environments significantly contribute to the mechanical behavior of the material.

Overall, the obtained results demonstrate that the structural properties of $CuMn_2O_4$ are strongly governed by subtle atomic-scale distortions and bonding characteristics. The good agreement between theoretical and experimental data validates the computational methodology and provides a solid basis for further investigations of spinel materials.

4.4.2.2. Electronic Properties

The spin-polarized band structures of $CuMn_2O_4$, calculated within the GGA and GGA+mBJ schemes are presented in Fig. 5 and Fig. 6. Within GGA approximation, a pronounced spin-dependent electronic response is obtained in one spin channel, the valence-band maximum reached the Fermi level (yielding essentially a zero band gap), while in the opposite spin channel, the bands cross the Fermi level. This indicates that $CuMn_2O_4$ is metallic with ferromagnetic character.

When the mBJ potential is included GGA+mBJ, $CuMn_2O_4$ retains a metallic character in one spin direction, whereas the other spin channel becomes semiconducting with an energy gap of 1.09 eV, confirming its half-metallic character.

This transition from a ferromagnetic metal (GGA) to a half-metallic ferromagnet (GGA+mBJ) demonstrates that the half-metallicity in $CuMn_2O_4$ is sensitive to the exchange–correlation treatment but becomes well stabilized when self-interaction errors are reduced. The resulting electronic structure yields 100% spin polarization at the Fermi level, which is a defining characteristic of half-metallic materials. This half-metallicity originates from the strong exchange splitting induced by the Cu and Mn cations occupying different crystallographic sites in the spinel structure. In the metallic spin channel, the states crossing the Fermi level are mainly derived from Mn-3*d* orbitals hybridized with O-2*p* states, while in the semiconducting spin channel the Cu-3*d* states are pushed away from the Fermi level due to crystal-field effects and exchange interactions.

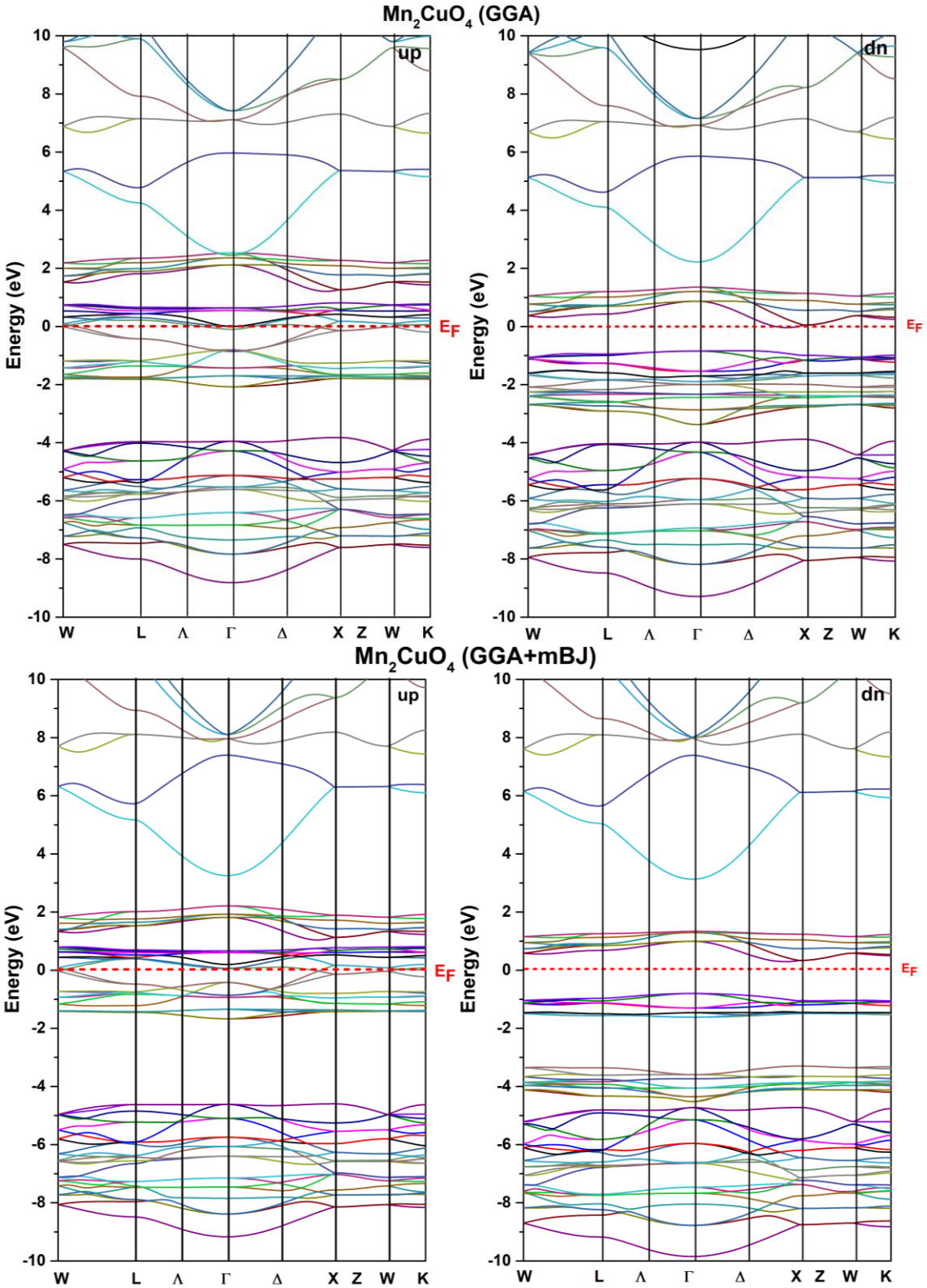

***Figure 4 4**: Spin-polarized band structures of Mn_2CuO_4 calculated using GGA and GGA+mBJ approximations*

5.

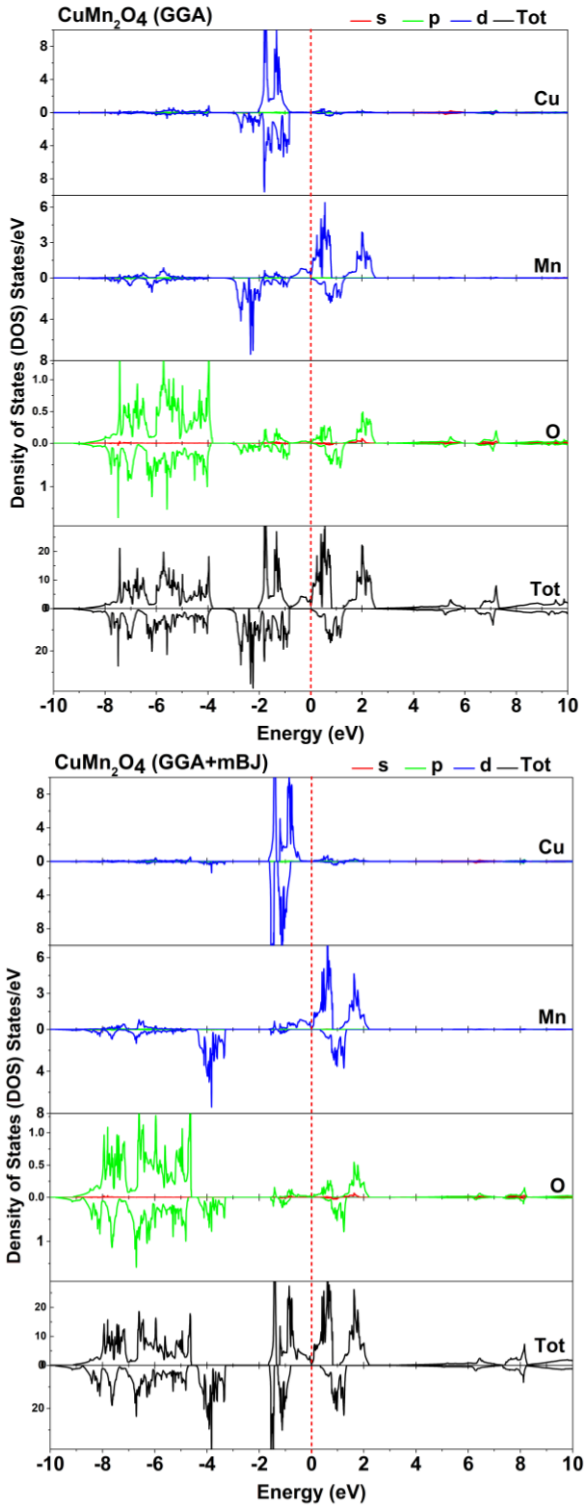

Figure 4 5: *Spin-polarized total and atomic densities of states for Mn_2CuO_4 calculated using GGA and GGA+mBJ approximations.*

4.4.2.3.Magnetic Properties

The calculated spin magnetic moments, as reported in **Table 2**, reveal a robust spin polarization consistent with the spin-resolved band structures. The integer total magnetic moments of 10 μ_B for $CuMn_2O_4$, indicates a quantized spin-dependent electronic structure, as expected for half-metallic systems.

The magnetization is mainly carried by Mn ions located on the octahedral sublattice. This observation is in agreement with the projected density of states (PDOS), which shows that Mn-3d states, hybridized with O-2p orbitals, dominate near the Fermi level. In contrast, the Cu magnetic moment inside the muffin-tin sphere remains relatively small, which can be attributed to strong covalency and partial delocalization of the magnetic moment.

Additionally, the interstitial region contributes non-negligibly to the total magnetization, indicating that a fraction of the spin density is delocalized outside the atomic spheres. This behavior is typical of transition metal oxides with significant hybridization between metal d-states and oxygen p-states.

Overall, the magnetic behavior of $CuMn_2O_4$ is governed by strong exchange interactions and spin polarization effects, leading to a stable half-metallic ferromagnetic state.

***Table 4- 3**: Calculated site-resolved spin magnetic moments (in μB) for $CuMn_2O_4$ spinel compound*

Compounds	Co	Cu	Mn	O	Interstitiel	Total
$CuMn_2O_4$	//	0.15337	2.20410	0.06841	0.32968	10.00007

References

1. Rafiq, M.A., et al., *Structural, electronic, magnetic and optical properties of AB2O4 (A= Ge, Co and B= Ga, Co) spinel oxides.* Materials Chemistry and Physics, 2021. **257**: p. 123794.
2. Kalia, S., R. Jasrotia, and V.P. Singh, *Magnetic Nanoferrites and Their Composites: Environmental and Biomedical Applications*. 2023: Elsevier.
3. Hachilif, A., et al., *Exploring ZnFeSnO4 double spinel: a thorough investigation of mechanical, dynamical, magneto-electronic properties and lattice thermal conductivity.* Computational Condensed Matter, 2024. **39**: p. e00915.
4. Liu, G., et al., *Thermodynamics and electronic structure characteristics of MFe2O4 with different spinel structures: A first-principles study.* Ceramics International, 2023. **49**(18): p. 29747–29754.
5. Flores-Lasluisa, J.X., et al., *Transition metal oxides with perovskite and spinel structures for electrochemical energy production applications.* Environmental Research, 2022. **214**: p. 113731.
6. Xu, H., et al., *Current and future trends for spinel-type electrocatalysts in electrocatalytic oxygen evolution reaction.* Coordination Chemistry Reviews, 2023. **475**: p. 214869.
7. Kwon, B.J., et al., *Design strategies of spinel oxide frameworks enabling reversible mg-ion intercalation.* Accounts of Chemical Research, 2023. **57**(1): p. 1–9.
8. Cario, L., B. Corraze, and E. Janod, *Physics and Chemistry of Chalcogenide Quantum Materials with Lacunar Spinel Structure.* Chemistry of Materials, 2025.
9. Bouhbou, M., et al., *Magnetic, half-metallicity and electronic studies of Cd1-xZnxCr2Se4 chromium selenospinels.* Journal of Magnetism and Magnetic Materials, 2019. **476**: p. 86–91.
10. Zeng, X., et al., *Atomic-level cation occupation and magnetic properties of Ce 3+-doped ZnFe 2 O 4 spinel ferrite.* RSC Advances, 2025. **15**(26): p. 20908–20915.
11. Stevanovic, V., M. d'Avezac, and A. Zunger, *Simple point-ion electrostatic model explains the cation distribution in spinel oxides.* Phys. Rev. Lett, 2010. **105**(7): p. 11–14.
12. Ahmed, M.G., et al., *Cation Migration-Induced Lattice Oxygen Oxidation in Spinel Oxide for Superior Oxygen Evolution Reaction.* Angewandte Chemie International Edition, 2025. **64**(9): p. e202416757.
13. Liao, X., et al., *Ni1-xZnxFe2O4 heterojunction composites derived from normal/inverse spinel structure for ppb-level acetone detection.* Sensors and Actuators B: Chemical, 2025. **436**: p. 137733.
14. Yesuraj, J., et al., *Construction of Ternary Zn0. 5Cu0. 5Co2O4 Spinel Structure on Nickel Foam: A Comprehensive Theoretical and Experimental Study from Single to Ternary Metal Oxides for High-Energy-Density Asymmetric Supercapacitor Application.* Small, 2025. **21**(10): p. 2407608.
15. Fang, D., et al., *Effect of CuMn 2 O 4 spinel in Cu–Mn oxide catalysts on selective catalytic reduction of NO x with NH 3 at low temperature.* Rsc Advances, 2014. **4**(49): p. 25540–25551.
16. Patra, P., et al., *Crossover from meta-magnetic state to spin-glass behaviour upon Ti-substitution for Mn in CuMn2O4.* Journal of Materials Science: Materials in Electronics, 2022. **33**(1): p. 554–564.
17. Hadded, A., et al., *Study of physical properties of a ferrimagnetic spinel Cu 1.5 Mn 1.5 O 4: spin dynamics, magnetocaloric effect and critical behavior.* RSC advances, 2021. **11**(41): p. 25664–25676.
18. Wan, X., et al., *A CuMn 2 O 4 spinel oxide as a superior catalyst for the aerobic oxidation of 5-hydroxymethylfurfural toward 2, 5-furandicarboxylic acid in aqueous solvent.* Catalysis Science & Technology, 2021. **11**(4): p. 1497–1509.
19. Blaha, P., et al., *Full-potential, linearized augmented plane wave programs for crystalline systems.* Computer physics communications, 1990. **59**(2): p. 399–415.

20. Danks, A.E., S.R. Hall, and Z. Schnepp, *The evolution of 'sol–gel'chemistry as a technique for materials synthesis.* Materials Horizons, 2016. **3**(2): p. 91–112.
21. Lin, J., et al., *Multiform oxide optical materials via the versatile pechini-type sol− gel process: synthesis and characteristics.* The Journal of Physical Chemistry C, 2007. **111**(16): p. 5835–5845.
22. Blügel, S. and G. Bihlmayer, *Full-potential linearized augmented planewave method.* Computational nanoscience: do it yourself, 2006. **31**: p. 85–129.
23. Orio, M., D.A. Pantazis, and F. Neese, *Density functional theory.* Photosynthesis research, 2009. **102**(2): p. 443–453.
24. Neugebauer, J. and T. Hickel, *Density functional theory in materials science.* Wiley Interdisciplinary Reviews: Computational Molecular Science, 2013. **3**(5): p. 438–448.
25. Blaha, P., et al., *wien2k.* An augmented plane wave+ local orbitals program for calculating crystal properties, 2001. **60**(1): p. 155–169.
26. Perdew, J.P., K. Burke, and M. Ernzerhof, *Generalized gradient approximation made simple.* Physical review letters, 1996. **77**(18): p. 3865.
27. Koller, D., F. Tran, and P. Blaha, *Improving the modified Becke-Johnson exchange potential.* Physical Review B—Condensed Matter and Materials Physics, 2012. **85**(15): p. 155109.
28. Yousef, R., et al., *Synthesis and characterisation of structural and electrical properties of CuMn2O4 spinel compound.* Journal of King Faisal University: Basic and Applied Sciences, 2021. **22**(2): p. 47–50.

CONCLUSIONS

CONCLSIONS

In this comprehensive investigation, we successfully demonstrated the crucial role of cation arrangement and transition-metal interactions in determining the structural, electronic, and magnetic properties of the spinel oxide $CuMn_2O_4$ through the combined use of experimental synthesis and first-principles FP-LAPW calculations within the GGA+mBJ framework. The successful preparation of single-phase cubic $CuMn_2O_4$ by the sol–gel method, together with the excellent agreement between experimental XRD refinements and theoretical structural optimization, confirms the reliability of the adopted computational and experimental approaches.

The electronic structure analysis revealed that $CuMn_2O_4$ exhibits a ferromagnetic half-metallic character, characterized by metallic behavior in one spin channel and semiconducting behavior in the opposite channel with a band gap of 1.09 eV. This half-metallic nature originates mainly from the strong hybridization between Cu-3d, Mn-3d, and O-2p states near the Fermi level, emphasizing the important contribution of transition-metal–oxygen interactions in controlling the electronic transport properties. Moreover, the calculated integer total magnetic moment of 10 μ_B provides clear evidence of complete spin polarization, confirming the suitability of $CuMn_2O_4$ for spintronic applications requiring highly spin-polarized currents.

Furthermore, the present study highlights the influence of Jahn–Teller distortions associated with Cu^{2+} ions on the stabilization of the magnetic and electronic ground state of the spinel lattice. The obtained results establish $CuMn_2O_4$ as a promising candidate for future spintronic devices such as spin injectors, magnetic tunnel junctions, and spin valves. Beyond its technological relevance, this work provides valuable insight into the interplay between crystal structure, magnetism, and electronic behavior in transition-metal spinels, offering a solid framework for the rational design of advanced functional oxide material

Abstract

This dissertation presents an experimental and theoretical study of the spinel oxide $CuMn_2O_4$. The compound was synthesized by the sol–gel method and structurally characterized by X-ray diffraction, confirming a single-phase cubic spinel structure. First-principles FP-LAPW calculations within the GGA+mBJ approximation were performed to investigate its electronic and magnetic properties. The results reveal that $CuMn_2O_4$ exhibits a ferromagnetic half-metallic behavior with a spin-dependent band gap of 1.09 eV and an integer magnetic moment of 10 μ_B, indicating complete spin polarization. The electronic and magnetic properties are mainly governed by the hybridization between Cu-3d, Mn-3d, and O-2p states and by the Jahn–Teller effect associated with Cu^{2+} ions. These findings highlight the potential of $CuMn_2O_4$ for spintronic applications

Résumé

Cette dissertation présente une étude expérimentale et théorique du spinelle $CuMn_2O_4$. Le composé a été synthétisé par la méthode sol–gel et caractérisé par diffraction des rayons X, confirmant une structure spinelle cubique monophasée. Des calculs FP-LAPW basés sur l'approximation GGA+mBJ ont été réalisés afin d'étudier ses propriétés électroniques et magnétiques. Les résultats montrent que $CuMn_2O_4$ possède un comportement demi-métallique ferromagnétique avec une bande interdite dépendante du spin de 1,09 eV et un moment magnétique entier de 10 μB, indiquant une polarisation de spin totale. Les propriétés électroniques et magnétiques sont principalement influencées par l'hybridation entre les états Cu-3d, Mn-3d et O-2p ainsi que par l'effet Jahn–Teller associé aux ions Cu^{2+}. Ces résultats soulignent le potentiel de $CuMn_2O_4$ pour les applications spintroniques.

ملخص

تقدم هذه المذكرة دراسة تجريبية ونظرية لمركب السبيني $CuMn_2O_4$. تم تحضير المركب باستعمال طريقة السول–جيل و توصيف بنيته بواسطة حيود الأشعة السينية، مما أكد تشكل بنية سبينيلية مكعبة أحادية الطور. كما أُجريت حسابات FP-LAPW ضمن تقريب GGA+mBJ لدراسة خصائصه الإلكترونية والمغناطيسية. أظهرت النتائج أن مركب $CuMn_2O_4$ يمتلك سلوكاً نصف فلزي حديدي المغناطيسية مع فجوة طاقوية معتمدة على اللف المغزلي قدرها 1.09 إلكترون فولت وعزم مغناطيسي كلي صحيح يساوي $10\ \mu_B$ ، مما يدل على استقطاب مغزلي كامل. وترجع هذه الخصائص إلى التهجين بين حالات Cu-3d و Mn-3d و O-2p إضافة إلى تأثير يان–تيلر المرتبط بأيونات Cu^{2+} وتبرز هذه النتائج إمكانيات المركب في تطبيقات السبينترونيك.